Master Thesis

How Effective is Battery Storage for Congestion Management in Dutch Low-Voltage Networks?

Author: T.G.J. Bredée (Thomas) (2672873)

1st supervisor: Alessandro Zocca
daily supervisor: Matthijs Riemersma (Accenture)
2nd reader: Rob van der Mei

A thesis submitted in fulfillment of the requirements for the VU Master of Science degree in Business Analytics

July 19, 2026

Abstract

The increasing electrification of residential energy consumption and the rapid deployment of rooftop photovoltaic (PV) systems are placing growing pressure on low-voltage electricity distribution networks. This thesis develops a mixed-integer linear programming model to determine the optimal placement, sizing, and operation of Battery Energy Storage Systems (BESS) for mitigating congestion in radial low-voltage networks. The model is based on the LinDistFlow approximation and explicitly considers network power flows, voltage limits, transformer and line capacities, battery operation, and PV curtailment over an hourly one-year horizon. The framework is evaluated on a SimBench distribution network using Dutch demand, PV generation, and electricity price data under multiple electrification, PV penetration, and PV placement scenarios. The results show that optimal battery placement is largely determined by network topology, while battery sizing adapts to increasing electrification and photovoltaic penetration, and the economic value of storage depends strongly on electricity market conditions.

Contents

List of Figures

List of Tables

1

Introduction

Driven by the European Green Deal, the Dutch electricity sector is undergoing a rapid transition towards a low-carbon energy system [1]. This transition is characterized by two simultaneous developments. On the supply side, residential photovoltaic (PV) systems are increasingly being deployed. On the demand side, the electrification of heating, household items, and personal transportation in the form of electric vehicles substantially increases electricity consumption. Together, these developments fundamentally alter the operation of electricity distribution networks, transforming them from predictable systems with unidirectional power flows into increasingly decentralized and dynamic infrastructures (1, 2, 3).

Although congestion affects both transmission and distribution networks, the challenges are particularly acute within low-voltage (LV) distribution systems (4). These networks were originally designed to deliver electricity from higher voltage levels towards passive consumers. The rapid growth of rooftop PV generation has introduced bidirectional power flows, while increasing electrification places additional stress on already heavily utilized distribution assets. As a result, Distribution System Operators (DSOs) are increasingly confronted with voltage violations, overloaded cables and transformers, and reduced connection capacity for new customers and renewable generation (1, 5). These technical limitations have become one of the principal bottlenecks of the Dutch energy transition, delaying the integration of renewable energy technologies and new electricity demand.

The severity of these constraints is commonly assessed through the concept of *Hosting Capacity* (HC), which describes the amount of distributed generation that can be connected without violating operational network limits. Rather than representing a single

[1]https://eur-lex.europa.eu/resource.html?uri=cellar:b828d165-1c22-11ea-8c1f-01aa75ed71a1.0002.02/DOC_1&format=PDF

physical constraint, hosting capacity is determined by multiple interacting factors, including voltage violations, thermal loading of cables and transformers, and voltage unbalance (6). Once these limits are exceeded, DSOs must either reinforce the network, restrict additional grid connections, or curtail renewable generation. Consequently, increasing hosting capacity has become one of the central objectives in modern distribution network planning.

Several approaches have been proposed to alleviate distribution network congestion. Conventional grid reinforcement through upgrading cables, transformers, and substations remains the most robust technical solution but requires substantial capital investment and long implementation times (6). Alternative operational measures include photovoltaic curtailment, which temporarily reduces renewable generation during congestion events (2), and demand-side flexibility programs that shift electricity consumption away from peak periods. While these strategies can postpone network reinforcement, they either reduce renewable energy utilization or require active participation from consumers.

Battery Energy Storage Systems (BESS) have therefore emerged as a promising alternative for increasing network flexibility (5, 7, 8, 9). By charging during periods of surplus generation and discharging during periods of high demand, BESS can reduce transformer loading, mitigate voltage violations, increase PV hosting capacity, and defer costly grid upgrades. Depending on the application, storage systems may be installed centrally near distribution transformers or distributed throughout the network close to end-users. Their operation can further be coordinated using optimization or advanced control strategies to maximize both technical and economic benefits (2, 10, 11).

Despite this potential, determining where batteries should be installed, how large they should be, and how they should be operated remains a complex optimization problem. These decisions are highly interdependent (9, 12, 13): the optimal battery size depends on its location within the network, while operational decisions depend on both network topology and time-varying electricity demand, PV generation, and electricity prices. At the same time, detailed low-voltage network data are rarely publicly available because Distribution System Operators generally treat network topology and asset information as confidential. Consequently, many existing studies either optimize only placement, only sizing, or only operational scheduling, often using simplified assumptions or limited case studies.

This thesis addresses these challenges by developing an optimization framework for the joint placement, sizing, and operation of Battery Energy Storage Systems in radial low-voltage distribution networks. A Mixed-Integer Linear Programming (MILP) model based on the LinDistFlow formulation is developed to explicitly represent active and reactive power flows, voltage constraints, transformer and line loading limits, battery investment decisions, and photovoltaic curtailment. The framework is evaluated on a representative SimBench low-voltage network using Dutch hourly demand profiles, photovoltaic generation profiles, and day-ahead electricity prices. Through extensive scenario analyses, the study investigates how increasing electrification, different photovoltaic deployment strategies, and electricity price variability influence both the technical effectiveness and economic viability of battery storage as a congestion mitigation strategy.

The central research question addressed in this thesis is therefore:

> How can Battery Energy Storage Systems (BESS) be optimally sized, placed, and operated to mitigate congestion in low-voltage electricity distribution networks under increasing photovoltaic generation and electrification?

The following sub-questions support this main research question:

- Sub-question 1: *How does the optimal placement and sizing of Battery Energy Storage Systems affect congestion, voltage profiles, and line loading in low-voltage distribution networks under increasing electrification and PV penetration?*
- Sub-question 2: *How sensitive are optimal BESS placement, sizing, and network performance to different photovoltaic deployment strategies?*
- Sub-question 3: *How does electricity price volatility influence the economic viability of Battery Energy Storage Systems in low-voltage distribution networks?*

The remainder of this thesis is organized as follows. Chapter 2 reviews the existing literature on congestion in low-voltage distribution networks, photovoltaic hosting capacity, Battery Energy Storage Systems, and optimization approaches for storage planning. Chapter 3 presents the mathematical optimization model. Chapter 4 describes the network data, modeling assumptions, and experimental design. Chapter 5 presents the experimental results for the three research questions. Chapter 6 discusses these findings, addresses the limitations of the study, and reflects on their implications. Finally, Chapter 7 concludes the thesis by summarizing the main findings and providing recommendations for future research, and addresses limitations.

2

Literature Review

2.1 Congestion in Low-Voltage Distribution Networks

The increasing electrification of residential energy demand and the rapid deployment of distributed photovoltaic (PV) systems have fundamentally altered the operating conditions of low-voltage (LV) distribution networks (6, 14) . Traditionally, these networks were designed for unidirectional power flows from centralized generation towards passive consumers. The growing presence of distributed generation and heightened electrification introduces new operational challenges, causing network components to operate closer to their technical limits. These limitations are commonly described through the concept of congestion, which occurs when one or more network constraints prevent the secure transport of electricity(11, 14).

Within the LV literature, congestion is frequently analyzed through the concept of *hosting capacity* (HC) (2, 6, 11), defined as the maximum amount of distributed generation that can be connected to a network without violating predefined technical limits. While hosting capacity is often presented as a single value, recent studies demonstrate that the underlying congestion mechanisms are considerably more complex (5).

Torquato et al. (2018) (6) performed one of the largest hosting-capacity assessments reported in the literature, analyzing approximately 50,000 real-world radial LV networks representing nearly 1.8 million customers. Their results showed that voltage-related constraints constitute the dominant limitation for PV deployment across most LV networks. In particular, overvoltage conditions consistently emerged before thermal limits of transformers or distribution lines were reached. Furthermore, the study demonstrated that hosting capacity follows a predictable statistical distribution across large populations of networks, suggesting that congestion patterns can be assessed at a portfolio level rather than solely on a feeder-by-feeder basis. These findings indicate that voltage management plays a central role in accommodating increasing levels of distributed PV generation.

While Torquato et al. (2018) identify voltage rise as the primary limiting factor in large populations of LV feeders, Fatima et al. (2021) (5) argue that the exact nature of congestion depends strongly on both network characteristics and the definition used to measure HC. Using stochastic Monte Carlo simulations on representative rural, suburban, and urban distribution networks, the authors compared multiple hosting-capacity references, including voltage rise, transformer loading, cable loading, and neutral conductor loading. Their results revealed substantial differences between network types. Rural networks exhibited the lowest hosting capacities due to long feeder lengths and relatively high line impedances, causing voltage violations to occur at comparatively low PV penetration levels. In contrast, urban networks generally supported considerably higher levels of PV generation before voltage constraints became active, shifting the dominant bottleneck towards transformer or cable loading.

Together, these studies suggest that congestion in LV networks cannot be characterized solely through thermal loading or transformer utilization. Instead, congestion emerges through the interaction between network topology, line impedance, voltage behavior, and local generation patterns. Although voltage rise is frequently identified as the most restrictive constraint under increasing PV penetration, the literature demonstrates that the dominant bottleneck remains highly dependent on local network conditions. Consequently, evaluating congestion mitigation strategies requires simultaneously considering both voltage and thermal network constraints.

2.2 Hosting Capacity and PV Integration

The increasing deployment of residential PV systems has transformed hosting capacity from a theoretical planning concept into a practical limitation faced by distribution network operators (5, 6). As PV penetration increases, the ability of low-voltage networks to accommodate additional generation becomes increasingly dependent on local network conditions, operational assumptions, and the spatial distribution of PV installations (15).

A recurring finding throughout the literature is that voltage rise constitutes one of the most significant barriers to further PV integration. Shabbir et al. (2) demonstrate that rapid residential PV adoption can cause both voltage violations and thermal overloading of network assets when local generation exceeds demand. Their analysis highlights the highly dynamic nature of hosting capacity, showing that network constraints are strongly influenced by the temporal mismatch between PV production and electricity consumption. In particular, periods of high solar generation combined with low local demand create conditions under which hosting-capacity limits are most likely to be exceeded.

Similar observations are reported by Yang et al. (11), who investigate the operational consequences of high PV penetration in distribution networks. The authors show that increasing PV generation simultaneously affects voltage regulation and peak-loading behavior throughout the network. Their results suggest that hosting-capacity limitations cannot be understood solely through instantaneous voltage violations, but must also be evaluated in the context of broader network operating conditions. Furthermore, the study emphasizes that the economic consequences of accommodating additional PV generation depend heavily on the severity and frequency of these technical constraints, highlighting the importance of realistic long-term assessments rather than purely technical worst-case analyses.

While both Shabbir et al. (2) and Yang et al. (11) primarily focus on the operational impacts of increasing PV penetration, Khalil et al. (7) demonstrate that hosting capacity is also strongly influenced by where PV generation is connected within the network. Their work shows that electrically weak locations, typically characterized by greater electrical distance from the substation and higher voltage sensitivity, experience congestion and voltage violations at lower levels of PV penetration than electrically stronger locations. Consequently, identical amounts of installed PV generation can result in substantially different network impacts depending on the allocation strategy used. These findings suggest that PV placement itself can be viewed as an important design variable when evaluating hosting capacity.

Taken together, these studies demonstrate that hosting capacity is not a fixed physical property of a distribution network. Instead, it emerges from the interaction between network topology, demand patterns, operational conditions, and the spatial distribution of PV generation. While Shabbir et al. (2) emphasize the importance of temporal variability in generation and demand, Yang et al. (11) highlight the broader operational consequences of high PV penetration, and Khalil et al. (7) show that PV placement decisions can significantly influence the severity of network constraints. Together, the literature suggests that evaluating PV integration requires considering not only how much PV is installed, but also when and where generation occurs within the network.

2.2.1 PV Placement and Network Sensitivity Metrics

Khalil et al. (7) demonstrate that the impact of photovoltaic generation on distribution network performance depends not only on the amount of installed PV capacity, but also on where this capacity is connected within the network. To account for this effect, the authors propose a placement strategy that prioritizes locations based on network sensitivity rather than allocating PV uniformly across all buses. Their results show that alternative deployment patterns can significantly influence voltage stability and the overall ability of the network to accommodate additional renewable generation.

To identify sensitive network locations, Khalil et al. (7) employ the Line Stability Index proposed by Salama et al. (16). This index quantifies the relative importance of individual network branches by measuring their sensitivity to changes in power flow conditions. Higher index values indicate lines that are more critical to maintaining stable network operation and therefore more susceptible to congestion and voltage-related problems. By allocating PV generation according to these sensitivity values, the methodology provides a systematic way to investigate how spatial deployment patterns influence network performance.

2.3 Battery Energy Storage Systems in Distribution Networks

Battery Energy Storage Systems (BESS) have emerged as one of the most widely studied flexibility technologies for addressing operational challenges in modern distribution networks. Unlike conventional grid reinforcement, which increases network capacity through physical infrastructure upgrades, battery storage provides operational flexibility by shifting energy across time. This enables batteries to respond dynamically to fluctuations in electricity demand and renewable generation, making them particularly attractive in low-voltage (LV) networks experiencing increasing electrification and PV penetration (2, 8, 11, 17).

The literature identifies several mechanisms through which BESS can support distribution network operation. One of the earliest applications is peak shaving, where batteries charge during periods of relatively low demand and discharge during periods of peak consumption. Wade et al. (17) demonstrate that such operation can substantially reduce loading on upstream transformers and network assets, thereby postponing or avoiding costly reinforcement investments. Similarly, Mazza et al. (8) show that storage can reduce feeder loading while simultaneously improving the utilization of existing infrastructure. These studies highlight that the value of BESS, as storage can directly contribute to congestion management within constrained distribution networks. Similar benefits are reported by Zhang et al. (3), who show that strategically deployed storage can improve both network reliability and voltage stability.

A second major application concerns the integration of distributed photovoltaic generation. As discussed in the previous section, high PV penetration often creates a temporal mismatch between local generation and electricity consumption. Shabbir et al. (2) show that excess midday PV production frequently coincides with periods of relatively low demand, causing voltage violations and transformer overloading that limit the hosting capacity of LV networks. Their results demonstrate that storage can reduce these effects by shifting surplus PV generation to later periods of the day when electricity demand is higher. Similarly, Yang et al. (11) investigate the interaction between PV generation and battery storage from both a technical and economic perspective. The authors argue that many previous studies implicitly assume oversized storage systems and therefore overestimate the benefits achievable in practice. By explicitly incorporating battery degradation and lifecycle costs, they show that economically viable storage systems can still provide meaningful reductions in voltage violations and peak loading, while improving the ability of the network to accommodate additional PV generation.

2.4 BESS Siting and Sizing Optimization

While BESS can provide a range of benefits to distribution networks, their effectiveness strongly depends on where they are installed and how large they are sized (1, 12, 18, 19). Consequently, a substantial body of literature focuses on the BESS siting and sizing problem, which seeks to determine the optimal battery locations and capacities that maximize technical and economic benefits while respecting network constraints.

A recurring finding throughout the literature is that battery placement has a significant influence on network performance. Yunusov et al. (1) demonstrate that storage located near the end of a radial feeder provides substantially greater voltage support than storage placed near the transformer. Because end-of-feeder locations are typically the most voltage-sensitive parts of the network, battery operation at these locations directly affects the buses most vulnerable to voltage violations. Similar conclusions are reported by Mazza et al. (8), who show that strategically located storage can simultaneously improve voltage profiles, reduce network losses, and alleviate local congestion. Inaolaji et al. (20) further observe that electrically weak locations often provide the highest marginal network value, reinforcing the importance of explicitly considering network topology during the siting process. Similar observations are reported by Wagle et al. (18), who show that network-aware storage placement can significantly improve congestion mitigation performance compared to uniformly allocated storage resources.

These findings have led to a distinction between centralized and distributed storage deployment strategies. Centralized batteries are typically installed near substations and on Medium Voltage networks and primarily target system-wide objectives such as transformer congestion relief and peak-load reduction. Distributed storage systems, in contrast, are installed at multiple LV locations throughout the feeder and are intended to address local voltage issues and congestion hotspots. Wade et al. (17) and Yunusov et al. (1) report that distributed deployment often provides greater technical benefits within LV networks because storage can directly influence local power flows and voltage conditions. However, these benefits must be balanced against increased coordination complexity and investment costs. As a result, the optimal deployment strategy depends strongly on the dominant network constraint, with thermal congestion often favoring centralized solutions and voltage-related constraints favoring more distributed configurations. With this study's focus on voltage-related problems due to increased PV penetration, a distributed approach is considered.

Beyond location selection, determining the appropriate battery size is equally important. Yang et al. (11) argue that many studies implicitly assume oversized storage systems capable of eliminating network constraints, despite such solutions being economically unrealistic. By incorporating battery degradation and lifecycle costs into the sizing problem, the authors demonstrate that appropriately sized storage systems can capture a large share of the available technical benefits while avoiding excessive investment costs. Similarly, Valencia et al. (21) formulate the sizing problem as a joint planning and operational optimization task, showing that battery power and energy capacities should be determined simultaneously with network operation rather than specified *a priori*. Rio-Mariani et al. (22) similarly emphasize the need to balance economic and technical objectives when determining battery capacities, demonstrating that optimal sizing depends strongly on the trade-off between investment costs and network benefits. Together, these studies suggest that battery sizing should be driven by the characteristics of the network, demand profile, and renewable generation patterns rather than by predetermined technology assumptions. Similar conclusions are reached by Jannesar et al. (9), who jointly optimize battery placement, sizing, and daily charging schedules. Their study demonstrates that coordinating these decisions leads to greater technical and economic benefits than optimizing battery size or location independently.

2.5 Distribution Network Optimization Models

The optimization of BESS in distribution networks requires a mathematical representation of electricity flows that accurately captures network behavior while remaining computationally tractable. As discussed in the previous section, battery placement, sizing, and operation are highly interdependent decisions. Consequently, modern optimization frameworks must simultaneously represent investment decisions, operational scheduling, and network constraints.

To solve these problems, the literature proposes a variety of optimization approaches. Mathematical programming techniques such as Mixed-Integer Linear Programming (MILP) and Mixed-Integer Nonlinear Programming (MINLP) are commonly employed because they can simultaneously capture investment decisions, operational scheduling, and network constraints (20, 21, 23, 24). Alternative approaches include metaheuristic methods such as Genetic Algorithms, which are applied when the optimization problem becomes highly nonlinear or computationally challenging. For example, Khaki et al. (25) employ a Genetic Algorithm to jointly optimize battery placement and sizing, demonstrating its ability to efficiently search large solution spaces where constraint modeling optimization techniques may become computationally burdensome. Regardless of the optimization method employed, all approaches ultimately depend on the underlying representation of power flows within the distribution network.

Several power flow formulations have been proposed in the literature, each offering a different balance between modeling accuracy and computational complexity. The most physically accurate representation is provided by Alternating Current Optimal Power Flow (AC-OPF) formulations, which explicitly model active power, reactive power, voltage magnitudes, and voltage angles through nonlinear power flow equations. Tang and Low (26) demonstrate how AC-OPF formulations can be applied to distribution network optimization while preserving the physical characteristics of electricity flows. However, the resulting optimization problems are computationally demanding, such that they only investigate a 12 node system.

To reduce computational complexity, simplified formulations are frequently adopted. One common approximation is Direct Current Optimal Power Flow (DC-OPF), which linearizes active power flows and is widely used in transmission system applications. Nevertheless, the assumptions underlying DC-OPF become less appropriate in low-voltage distribution networks, where voltage constraints frequently constitute the dominant operational limitation and line resistances are relatively large compared to transmission systems (5, 6). As a result, models that neglect voltage behavior and reactive power flows may fail to capture the network characteristics most relevant to LV planning studies.

To overcome these limitations, many studies adopt DistFlow-based formulations originally developed by Baran and Wu (27). Their work introduced a power flow representation specifically designed for radial distribution feeders, explicitly incorporating active power flows, reactive power flows, and voltage behavior. As a result, DistFlow formulations provide a much closer representation of physical network behavior than transport-based or DC approximations while remaining more computationally tractable than full AC models.

Building upon this framework, linearized DistFlow formulations, commonly referred to as LinDistFlow models, simplify the nonlinear DistFlow equations into a set of linear relationships suitable for optimization. These formulations have become increasingly popular in studies involving distributed generation, hosting capacity assessment, and battery storage planning (28). Fortenbacher et al. (29) show that storage placement and sizing decisions should be evaluated within a network-constrained optimization framework. Their work illustrates the need for models that capture network behavior while remaining computationally manageable. Similarly, Aghaei et al. (13) emphasize the role of flexibility resources within active distribution networks and show that optimization models must explicitly account for network constraints when evaluating flexibility investments. Iria et al. (30) further argue that investment and operational decisions should be optimized simultaneously, requiring formulations that remain computationally efficient despite the inclusion of detailed network representations.

Consequently, LinDistFlow formulations have emerged as a practical compromise between physical realism and computational efficiency. By retaining voltage constraints and reactive power flows while preserving linearity, these models enable the simultaneous optimization of network operation and investment decisions using MILP techniques (10, 20, 21, 31). This capability is particularly important in studies involving battery placement and sizing, where thousands of operational decisions must be evaluated alongside discrete investment choices.

Given the focus of this thesis on battery placement, battery sizing, and network-constrained operation within a radial low-voltage distribution network, a LinDistFlow formulation is adopted. This approach allows voltage limits, line loading constraints, photovoltaic generation, and battery operation to be represented within a single optimization framework while maintaining computational tractability for a full-year optimization horizon.

2.6 Battery Operational Models

In addition to determining where batteries should be installed and how large they should be, the literature also emphasizes the importance of accurately modeling battery operation. The operational behavior of a Battery Energy Storage System determines when energy is stored, when it is released, and how effectively the battery can provide network support. Consequently, battery operation plays a central role in evaluating the economic and technical value of storage investments.

Most battery optimization models represent battery operation through a state-of-charge (SOC) variable that tracks the amount of energy stored within the system over time. The SOC evolves according to charging and discharging decisions while accounting for conversion losses associated with battery efficiency (20, 21). To preserve battery lifetime and ensure realistic operation, minimum and maximum SOC limits are commonly imposed, preventing deep discharge and overcharging (11). These constraints reflect practical operating limits that are widely used in commercial lithium-ion battery systems.

Another important modeling choice concerns battery degradation. Repeated charging and discharging gradually reduce the usable capacity of a battery, creating an operational cost that should be considered when evaluating storage investments. The literature proposes several approaches to account for degradation, ranging from detailed electrochemical ageing models to simplified throughput-based cost approximations (11). Because detailed degradation models often introduce significant computational complexity, many optimization studies employ linear degradation costs that are proportional to the amount of energy cycled through the battery (20).

The economic representation of battery investments also varies across the literature. A common approach is to separate battery costs into an energy-related component, expressed in EUR/kWh, and a power-related component, expressed in EUR/kW (10, 20). This distinction allows the optimization model to independently determine the most suitable energy capacity and converter power rating. Since battery investments are long-term decisions, these capital costs are frequently annualized through a capital recovery factor, enabling direct comparison with yearly operational costs and benefits.

Finally, operational battery models often include a predefined relationship between energy capacity and power capacity. Several studies assume fixed-duration battery systems, where the battery can discharge at rated power for a specified number of hours (8). This approach reduces model complexity while ensuring realistic sizing decisions. Collectively, these modeling choices provide the foundation for representing battery operation within optimization frameworks and are incorporated into the mathematical model developed in this thesis.

2.7 Literature Synthesis and Research Gap

The literature demonstrates that BESS have significant potential to improve the flexibility of low-voltage distribution networks by reducing congestion, mitigating voltage violations, and increasing the utilization of distributed photovoltaic generation. At the same time, existing research consistently shows that the effectiveness of battery storage depends on a combination of technical and economic factors, including network topology, battery placement, sizing decisions, operational strategies, and the spatial distribution of photovoltaic systems. Although considerable progress has been made, several limitations remain. Many studies investigate only a subset of these decisions, rely on simplified network representations or short simulation horizons, or evaluate a single PV deployment scenario, making it difficult to assess the robustness of optimal BESS investments under changing network conditions. Furthermore, relatively little research has focused on Dutch low-voltage distribution networks using realistic demand, generation, and electricity price profiles over an entire year.

To address these research gaps, this thesis develops an optimization framework that simultaneously determines the optimal placement, sizing, and operation of BESS within a realistic radial low-voltage distribution network. The model incorporates explicit voltage and line-loading constraints through a LinDistFlow formulation and evaluates battery performance under increasing electrification levels, alternative photovoltaic deployment strategies, and varying electricity market conditions. The following chapters describe the mathematical formulation, case study design, and experimental methodology used to answer the research questions introduced in Chapter 1.

3

Mathematical Model

This chapter presents the mathematical optimization model developed for the optimal placement, sizing, and operation of BESS in a radial low-voltage distribution network with photovoltaic (PV) generation.

The optimization problem is formulated as a Mixed-Integer Linear Program (MILP), combining battery investment decisions with network-constrained operational scheduling. The model simultaneously determines: where batteries should be installed, how large their power and energy capacities should be, how batteries should charge and discharge over time, how PV generation should be utilized or curtailed, and how active and reactive power should flow through the network.

To capture electrical network behavior, a linearized DistFlow (LinDistFlow) formulation is adopted. This allows active power flows, reactive power flows, and voltage magnitudes to be modeled while preserving linearity. Apparent power limits of lines and PV inverters are represented using polygonal linear approximations, ensuring compatibility with MILP solvers.

The objective is to minimize the total annual system cost, which consists of electricity purchase costs, battery investment costs, battery degradation costs, and PV curtailment penalties, while satisfying all operational and network constraints.

3.1 Sets, Parameters, and Decision Variables

The optimization model is defined on a radial low-voltage distribution network represented by a graph, with a parent-tree such that every node only has one parent. The network consists of a set of buses, connecting lines, and a finite set of time intervals. Battery placement, sizing, and operation are optimized jointly with power flows and photovoltaic

Symbol	Meaning	Domain
$\mathcal{B}$	Set of non-substation buses	–
$\mathcal{B}_0$	Set of all buses including the substation	$\mathcal{B} \cup \{s\}$
$\mathcal{L}$	Set of radial lines oriented parent-to-child	(i, j)
$\mathcal{T}$	Set of time intervals	t
$\mathcal{C}(i)$	Set of children of bus i	–

Table 3.1: Model sets.

(PV) utilization. The following tables define the basis of the model, for the sets (Table 3.1), parameters (Table 3.2) and decision variables(Table 3.3).

Symbol	Meaning	Unit
r_{ij}	Line resistance of $(i,j) \in \mathcal{L}$	p.u.
x_{ij}	Line reactance of $(i,j) \in \mathcal{L}$	p.u.
$S_{ij}^{\max}$	Apparent power capacity of line (i,j)	p.u.
$v^{\min}, v^{\max}$	Squared voltage limits	p.u.^{2}
$p_{i,t}^{D}$	Active demand at bus i at time t	p.u.
$q_{i,t}^{D}$	Reactive demand at bus i at time t	p.u.
$p_{i,t}^{PV}$	Available PV generation at bus i at time t	p.u.
S_{i}^{inv}	PV inverter apparent power rating	p.u.
c_t	Electricity price at time t	EUR/kWh
c_P	Battery power investment cost	EUR/kW
c_E	Battery energy investment cost	EUR/kWh
α	Battery investment annuity factor	–
$c_{\deg}$	Battery degradation cost per kWh throughput	EUR/kWh
c_t^{curt}	PV curtailment penalty at time t	EUR/kWh
η	Battery one-way efficiency	–
Δt	Time step duration	h
$SOC^{\min}, SOC^{\max}$	Minimum and maximum battery SOC limits	–
E^{CAP}	Big-M upper-bound on battery energy capacity	p.u.

Table 3.2: Model parameters.

Symbol	Meaning	Domain
$P_{ij,t}$	Active power flow on line (i,j)	$\mathbb{R}$
$Q_{ij,t}$	Reactive power flow on line (i,j)	$\mathbb{R}$
$P_{s,t}^{sub}$	Active power exchanged at substation	$\mathbb{R}_{\geq 0}$
$Q_{s,t}^{sub}$	Reactive power exchanged at substation	$\mathbb{R}_{\geq 0}$
$v_{i,t}$	Squared voltage magnitude at bus i	$\mathbb{R}_{\geq 0}$
b_i	Battery installation decision	$\{0,1\}$
P_i^{max}	Battery power capacity	$\mathbb{R}_{\geq 0}$
E_i^{max}	Battery energy capacity	$\mathbb{R}_{\geq 0}$
$p_{i,t}^{CHA}$	Battery charging power	$\mathbb{R}_{\geq 0}$
$p_{i,t}^{DIS}$	Battery discharging power	$\mathbb{R}_{\geq 0}$
$E_{i,t}$	Battery state of charge	$\mathbb{R}_{\geq 0}$
$p_{i,t}^{PV,used}$	Locally utilized PV power	$\mathbb{R}_{\geq 0}$
$p_{i,t}^{PV,curt}$	Curtailed PV power	$\mathbb{R}_{\geq 0}$
$q_{i,t}^{PV}$	Reactive PV power injection	$\mathbb{R}$

Table 3.3: Decision variables.

3.2 Objective Function

The objective of the model is to minimize the total annual system cost expressed in Eur (€) per year. This magnitude is chosen to avoid discrepancies in the magnitudes between the 4 objective parts. The objective function (3.1), consists of electricity purchase costs, annualized battery investment costs, battery degradation costs, and PV curtailment penalty costs.

$$\begin{aligned} \min \quad & \underbrace{\sum_{t\in\mathcal{T}} c_t S^{base} P^{sub}_{s,t} \Delta t}_{\text{(I) Energy cost}} \\ & \underbrace{+ \alpha \sum_{i\in\mathcal{B}} \left(c_P S^{base} P^{max}_i + c_E S^{base} E^{max}_i \right)}_{\text{(II) Annualized battery investment}} \\ & \underbrace{+ c_{\text{deg}} \sum_{i\in\mathcal{B}} \sum_{t\in\mathcal{T}} S^{base} \left(p^{CHA}_{i,t} + p^{DIS}_{i,t} \right) \Delta t}_{\text{(III) Battery degradation}} \\ & \underbrace{+ \sum_{i\in\mathcal{B}} \sum_{t\in\mathcal{T}} c^{curt}_t S^{base} p^{PV,curt}_{i,t} \Delta t}_{\text{(IV) PV curtailment cost}} . \end{aligned} \tag{3.1}$$

Here, all electrical decision variables are expressed in per-unit. Therefore, the base power S^{base} is included in each cost term to convert per-unit power and energy quantities back to physical units before multiplying them by economic parameters. In the implementation, $S^{base} = 1000$ kVA (= 1 MVA). This conversion ensures that all four objective terms are expressed in EUR per year.

(I) Energy cost The first term represents the cost of electricity exchanged with the upstream transmission grid through the substation.

The variable $P^{sub}_{0,t}$ denotes the active power imported at the substation in per-unit. Since optimization is performed in p.u., this quantity must be converted back to physical power by multiplying with the system base power of 1 MVA. Multiplication by the timestep duration Δt converts power (kW) into energy (kWh). Finally, the time-dependent electricity price c_t (EUR/kWh) converts energy consumption into monetary cost:

$$c_t \cdot P^{sub}_{s,t} S_{\text{base}} \Delta t \;\rightarrow\; \text{EUR}$$

The scalar c_t therefore acts as a temporal weighting factor, encouraging battery charging during low-price hours and battery discharging during expensive periods. This creates opportunities that allow the optimizer to shift energy consumption in time.

(II) Annualized battery investment The second term represents the annualized capital expenditure associated with battery installation and sizing. Since battery investments are incurred upfront but provide value over multiple years, the total capital cost is converted into an equivalent annual cost using the annuity factor α.

For each candidate bus $i \in \mathcal{B}$, the model optimizes both the battery power rating $P_i^{\max}$ (p.u.) and the energy capacity $E_i^{\max}$ (p.u.). These correspond to the converter power capability and nominal storage capacity, respectively. The total battery investment cost consists of two components:

$$c_P P_i^{\max} + c_E E_i^{\max},$$

where c_P denotes the power-related investment cost (EUR/kW), and c_E denotes the energy-related investment cost (EUR/kWh).

As all optimization variables are expressed in per-unit, the conversion back to physical units is again obtained by multiplication with the system base power:

$$c_P \cdot P_i^{\max} S_{\text{base}} \;+\; c_E \cdot E_i^{\max} S_{\text{base}} \;\rightarrow\; \text{EUR}.$$

To compare capital expenditure directly with yearly operational savings, the total battery cost is annualized using the capital recovery factor:

$$\alpha = \frac{r(1+r)^L}{(1+r)^L - 1},$$

where r is the discount rate and L is the battery lifetime in years. This transforms the one-time investment into an equivalent annual payment:

$$\alpha \left(c_P P_i^{\max} + c_E E_i^{\max} \right).$$

The scalar α therefore acts as a temporal normalization factor, ensuring that long-term investment decisions are economically comparable to annual operational costs. Without this correction, battery investment costs would be overrepresented relative to yearly electricity savings, leading to unrealistically conservative installation decisions.

(III) Battery degradation cost The third objective term captures the operational degradation of the battery caused by repeated charging and discharging. Lithium-ion batteries experience gradual capacity loss as energy throughput accumulates, meaning each cycle consumes a portion of the battery's remaining economic lifetime.

To approximate this effect, degradation is modeled as a linear cost proportional to total battery throughput:

$$c_{\text{deg}} \sum_{i \in \mathcal{B}} \sum_{t \in \mathcal{T}} \left(p_{i,t}^{CHA} + p_{i,t}^{DIS} \right) \Delta t.$$

The variables $p_{i,t}^{CHA}$ and $p_{i,t}^{DIS}$ denote battery charging and discharging power at bus i and time t, both expressed in per-unit. Multiplication by the timestep duration Δt converts instantaneous power into exchanged energy:

$$\left(p_{i,t}^{CHA} + p_{i,t}^{DIS} \right) S_{\text{base}} \Delta t \;\rightarrow\; \text{kWh}.$$

The degradation coefficient c_{deg} (EUR/kWh) represents the monetary value of battery wear per unit of energy throughput and is derived from the battery energy cost:

$$c_{\text{deg}} = \frac{c_E}{2 N_{\text{cycles}}},$$

where N_{cycles} denotes the expected cycle life of the battery. The factor of two appears because one full charge-discharge cycle corresponds to approximately $2E_i^{\max}$ of total throughput.

The scalar c_{deg} acts as a penalty on excessive cycling, preventing unrealistic battery dispatch patterns where arbitrage opportunities would otherwise incentivize continuous charging and discharging. This encourages the optimizer to use storage only when the economic benefit exceeds the implicit cost of battery wear.

(IV) PV curtailment cost The final objective term penalizes photovoltaic (PV) generation that cannot be locally consumed or stored under the no-export assumption and must therefore be curtailed.

The variable $p_{i,t}^{PV,curt}$ denotes curtailed PV power at bus i and time t, expressed in per-unit. Similar to the previous objective components, multiplication by S_{base} and Δt converts this quantity into curtailed energy:

$$p_{i,t}^{PV,curt} S_{\text{base}} \Delta t \;\rightarrow\; \text{kWh}.$$

The corresponding objective contribution is determined by the curtailment coefficient c_t^{curt}:

$$c_t^{curt}\, p_{i,t}^{PV,curt}\, S_{\mathrm{base}}\, \Delta t.$$

The curtailment coefficient is defined as

$$c_t^{curt} = \max(c_t, 0),$$

such that curtailed PV energy is therefore penalized using the electricity price whenever prices are positive. Because electricity export is disabled in this study, this term does not represent lost export revenue. Instead, it is a modeling penalty that places a value on renewable energy that cannot be used locally or stored in the battery. This encourages the optimization model to minimize PV curtailment while remaining consistent with the no-export assumption.

The curtailment penalty therefore provides an incentive to maximize local PV utilization. In combination with battery flexibility, it encourages the optimizer to store surplus PV generation during periods of high solar production rather than curtailing it. Consequently, battery placement and sizing are influenced not only by network constraints, but also by the objective of reducing renewable energy losses within the assumed no-export operating regime.

3.3 Network Energy Balance and Power Flow Constraints

To accurately represent physical power transport within the low-voltage distribution network, the optimization model adopts the LinDistFlow formulation introduced by Baran and Wu (27). This formulation explicitly models active and reactive power flows, voltage magnitudes, and network capacity limits while preserving linearity.

The network is assumed radial, such that each non-substation bus has exactly one parent node and zero or more downstream child nodes. Power flows are therefore oriented from parent to child, while negative values naturally represent reverse flow due to distributed generation.

Active power balance For every non-substation bus $j \in \mathcal{B}$ and timestep $t \in \mathcal{T}$, active power balance is enforced as:

$$P_{\pi(j),j,t} - \sum_{k\in\mathcal{C}(j)} P_{j,k,t} = p^{D}_{j,t} - p^{PV,used}_{j,t} + p^{CHA}_{j,t} - p^{DIS}_{j,t}, \tag{3.2}$$

where $P_{\pi(j),j,t}$ denotes active power flowing into bus j from its parent node, and $\sum_{k\in\mathcal{C}(j)} P_{j,k,t}$ represents active power distributed to downstream child buses.

The right-hand side captures the net active demand at bus j, consisting of electricity demand $p^{D}_{j,t}$, reduced by locally utilized photovoltaic generation $p^{PV,used}_{j,t}$, increased by battery charging demand $p^{CHA}_{j,t}$, and reduced by battery discharge supply $p^{DIS}_{j,t}$.

Constraint (3.2) ensures conservation of active power at every node and determines how energy is transported throughout the radial feeder.

Reactive power balance Reactive power balance is enforced analogously for every bus $j \in \mathcal{B}$:

$$Q_{\pi(j),j,t} - \sum_{k\in\mathcal{C}(j)} Q_{j,k,t} = q^{D}_{j,t} - q^{PV}_{j,t}, \tag{3.3}$$

where $Q_{\pi(j),j,t}$ and $Q_{j,k,t}$ denote incoming and outgoing reactive power flows, respectively.

The reactive demand $q^{D}_{j,t}$ is partially offset by reactive power support from photovoltaic inverters $q^{PV}_{j,t}$. Batteries are assumed to operate at unity power factor and therefore do not contribute reactive power.

Constraint (3.3) ensures conservation of reactive power and enables the model to capture voltage effects caused by both active and reactive injections.

Substation active power injection The total active power exchanged with the upstream transmission grid is determined by the aggregate active flow on all outgoing feeder lines connected to the substation:

$$P^{sub}_{s,t} = \sum_{k\in\mathcal{C}(0)} P_{s,k,t}, \tag{3.4}$$

where $P^{sub}_{0,t}$ denotes active power imported from or exported to the external grid.

Constraint (3.4) links the internal distribution network to the objective function, where electricity purchase costs are evaluated.

Substation reactive power injection Similarly, total reactive power exchanged at the substation is given by:

$$Q_{s,t}^{sub} = \sum_{k \in \mathcal{C}(0)} Q_{s,k,t}, \tag{3.5}$$

where $Q_{0,t}^{sub}$ represents reactive power drawn from or supplied to the upstream grid.

Constraint (3.5) ensures consistency between feeder-level reactive flows and external grid interaction.

Voltage drop along network lines Voltage propagation through the network is modeled using the linearized LinDistFlow voltage equation:

$$v_{j,t} = v_{i,t} - 2\left(r_{ij} P_{ij,t} + x_{ij} Q_{ij,t}\right), \qquad \forall (i,j) \in \mathcal{L}, \tag{3.6}$$

where $v_{i,t}$ and $v_{j,t}$ denote squared voltage magnitudes in p.u.^{2}, while r_{ij} and x_{ij} are the per-unit resistance and reactance of line (i,j).

Constraint (3.6) determines how voltage evolves along the feeder. Positive downstream power flow causes voltage decline, while reverse flow from excess PV generation can induce voltage rise.

Substation slack voltage To provide a voltage reference for the entire network, the substation voltage is fixed at:

$$v_{s,t} = (1.025)^2, \qquad \forall t \in \mathcal{T}, \tag{3.7}$$

which reflects the external grid voltage setpoint specified in the SimBench network data.

Constraint (3.7) acts as the slack boundary condition required for the LinDistFlow equations to be well-posed.

Voltage operating limits To ensure acceptable power quality, bus voltages must remain within predefined lower and upper bounds:

$$v_{\min} \leq v_{i,t} \leq v_{\max}, \qquad \forall i \in \mathcal{B}, \tag{3.8}$$

where $v_{\min} = 0.95^2$ and $v_{\max} = 1.05^2$.

Constraint (3.8) prevents undervoltage and overvoltage violations and constitutes one of the principal operational constraints in low-voltage networks with high photovoltaic penetration.

Line apparent power limits Each network line is subject to a thermal apparent power limit. To preserve linearity, the circular apparent-power constraint is approximated by a polygon with $K = 8$ supporting hyperplanes:

$$P_{ij,t} \cos(\theta_k) + Q_{ij,t} \sin(\theta_k) \leq S_{ij}^{\max}, \qquad \forall (i,j) \in \mathcal{L}, \quad k = 0, \ldots, K-1, \tag{3.9}$$

with

$$\theta_k = \frac{2\pi k}{K}.$$

Here, $S_{ij}^{\max}$ denotes the apparent power rating of line (i, j).

Constraint (3.9) provides a computationally efficient linear approximation of the circular apparent-power capability curve. Because the polygon is constructed using supporting hyperplanes, the resulting feasible region forms a circumscribing polygon around the true circular boundary. Consequently, the approximation may permit apparent power flows that slightly exceed the exact thermal rating. For the chosen value of $K = 8$, the maximum approximation error is approximately 8.2%. This trade-off is accepted to maintain computational tractability while preserving a close approximation of the nonlinear apparent-power limit.

Transformer Representation The distribution network is connected to the upstream transmission system through a single transformer located between the slack bus and the root node of the radial feeder. The transformer is assigned a series impedance and an apparent power limit, which is enforced on the line between the slack bus and the root node. The apparent power rating is denoted by $S_{\text{trafo}}^{\max}$ and is enforced through the same polygonal apparent-power approximation used for the distribution lines. Consequently, the power flow through the transformer is constrained by

$$\sqrt{\left(P_{s,t}^{sub}\right)^2 + \left(Q_{s,t}^{sub}\right)^2} \leq S_{\text{trafo}}^{\max}, \qquad \forall t \in \mathcal{T}.$$

The transformer impedance is incorporated into the network using a common per-unit base, allowing it to be represented as an equivalent series impedance without explicitly modelling transformer turns ratios. This approach ensures that both transformer loading and transformer voltage drops are included in the network constraints while maintaining the linear structure of the LinDistFlow formulation.

3.4 Photovoltaic Constraints

The photovoltaic (PV) part is modeled to capture both active power utilization and optional reactive power support. At each bus, available PV generation can either be consumed locally or curtailed, while inverter operating limits determine the feasible combination of active and reactive power injection.

Depending on the selected operating mode, PV inverters either provide reactive voltage support or operate at unity power factor.

PV power splitting For every bus $i \in \mathcal{B}$ and timestep $t \in \mathcal{T}$, the available photovoltaic generation must be allocated between utilized generation and curtailed generation:

$$p_{i,t}^{PV,used} + p_{i,t}^{PV,curt} = p_{i,t}^{PV}, \tag{3.10}$$

where $p_{i,t}^{PV}$ denotes the total available photovoltaic power, $p_{i,t}^{PV,used}$ the portion injected into the local network, and $p_{i,t}^{PV,curt}$ the portion that is curtailed.

Constraint (3.10) ensures energy conservation within the PV subsystem by requiring all generated solar power to be either utilized or curtailed. Curtailment occurs when network constraints, such as voltage limits or line thermal limits, prevent full local utilization of available generation.

The curtailed power $p_{i,t}^{PV,curt}$ directly contributes to the curtailment penalty term in the objective function, incentivizing the optimizer to maximize renewable self-consumption whenever feasible.

PV inverter apparent power limits When reactive power support is enabled, photovoltaic inverters may inject or absorb reactive power to support voltage regulation. However, the total inverter output remains limited by its apparent power rating.

This operating region is approximated using the same polygonal formulation as the line capacity constraints, see Constraint (3.9):

$$p_{i,t}^{PV,used} \cos(\theta_k) + q_{i,t}^{PV} \sin(\theta_k) \leq S_i^{inv}, \qquad \forall i \in \mathcal{B}, \quad k = 0, \ldots, K-1, \tag{3.11}$$

with

$$\theta_k = \frac{2\pi k}{K}.$$

Here, $q_{i,t}^{PV}$ denotes reactive power supplied or absorbed by the inverter, and S_i^{inv} represents the inverter apparent power capacity.

Constraint (3.11) approximates the feasible active–reactive operating envelope of the inverter. When active PV generation approaches its maximum output, less reactive power support remains available. Conversely, during lower active generation periods, additional reactive flexibility can be used for voltage regulation.

This capability allows the optimizer to trade off active energy injection and reactive voltage support, potentially reducing voltage violations and minimizing the need for PV curtailment.

Unity power factor operation In scenarios where reactive power support is disabled, PV inverters are constrained to operate at unity power factor:

$$q_{i,t}^{PV} = 0, \qquad \forall i \in \mathcal{B}, \quad t \in \mathcal{T}. \tag{3.12}$$

Constraint (3.12) removes reactive power flexibility entirely, restricting PV systems to active power injection only.

This scenario serves as an important benchmark for evaluating the value of inverter-based reactive support. Comparing optimization results between Constraint (3.11) and Constraint (3.12) reveals how much voltage management and curtailment reduction can be achieved through reactive PV control.

3.5 Battery Energy Storage Constraints

Battery installation budget To limit the total number of battery systems deployed in the network, the following budget constraint is imposed:

$$\sum_{i \in \mathcal{B}} b_i \leq N_{\mathrm{bat}}^{\max}, \tag{3.13}$$

where $b_i \in \{0, 1\}$ is a binary decision variable indicating whether a battery is installed at bus i, and $N_{\mathrm{bat}}^{\max}$ denotes the maximum number of batteries allowed in the system.

Constraint (3.13) controls the placement decision by restricting the number of selected battery locations. This enables scenario analysis under limited deployment budgets and reflects practical investment constraints.

State-of-charge dynamics Battery energy evolves over time according to charging and discharging decisions:

$$E_{i,t} = E_{i,t-1} + \eta\, p_{i,t}^{CHA} \Delta t - \frac{1}{\eta} p_{i,t}^{DIS} \Delta t, \qquad \forall i \in \mathcal{B}, \quad t \in \mathcal{T} \setminus \{t_0\}, \tag{3.14}$$

where $E_{i,t}$ denotes the battery state of charge (SOC), $p_{i,t}^{CHA}$ and $p_{i,t}^{DIS}$ are charging and discharging power, Δt is the timestep duration, and η is the one-way battery efficiency.

The charging term is multiplied by η, reflecting that only part of the imported electrical energy is stored internally. Conversely, discharging requires division by η, since delivering useful energy to the network consumes more stored energy than is ultimately exported.

Constraint (3.14) ensures physically consistent battery behavior and captures round-trip energy losses. No fixed initial SOC is imposed, allowing the optimizer to determine the most advantageous starting battery level.

Cyclic state-of-charge condition To prevent artificial depletion or overcharging at the boundaries of the optimization horizon, the battery is required to end the year at the same state of charge at which it began:

$$E_{i,t_T} = E_{i,t_0}, \qquad \forall i \in \mathcal{B}, \tag{3.15}$$

where t_0 and t_T denote the first and final timestep, respectively.

Constraint (3.15) enforces long-term energy neutrality and ensures that battery operation does not exploit unrealistic end-of-horizon effects. In the current implementation, the first-timestep charging and discharging decisions are not explicitly included in the wraparound update; this minor indexing issue is further discussed in Section 6.5.

Minimum state-of-charge limit To avoid excessive battery depletion and preserve operational lifetime, a minimum allowable SOC is enforced:

$$E_{i,t} \geq \sigma_{\min} E_i^{\max}, \qquad \forall i \in \mathcal{B}, \quad t \in \mathcal{T}, \tag{3.16}$$

where $\sigma_{\min}$ denotes the minimum allowable SOC fraction.

Constraint (3.16) ensures that a reserve level of stored energy is maintained, protecting the battery against deep discharge and associated degradation.

Maximum state-of-charge limit Similarly, battery charging is restricted by an upper SOC limit:

$$E_{i,t} \leq \sigma_{\max} E_i^{\max}, \qquad \forall i \in \mathcal{B}, \quad t \in \mathcal{T}, \tag{3.17}$$

where $\sigma_{\max}$ denotes the maximum usable SOC fraction.

Constraint (3.17) prevents overcharging and reflects practical battery operating windows, which are typically narrower than the full nominal capacity to improve longevity.

Battery discharge/charge power limit Battery discharging power is bounded by the installed inverter power rating, where $P_i^{\max}$ denotes the maximum battery power capacity.

$$p_{i,t}^{DIS} \leq P_i^{\max}, \qquad \forall i \in \mathcal{B}, \quad t \in \mathcal{T}, \tag{3.18}$$

Respectively, battery charging power is bounded by:

$$p_{i,t}^{CHA} \leq P_i^{\max}, \qquad \forall i \in \mathcal{B}, \quad t \in \mathcal{T}, \tag{3.19}$$

Constraints (3.18 & 3.19) guarantee feasible discharging and charging operation.

Battery power–energy coupling To enforce a fixed battery duration, installed power and energy capacity are linked through:

$$P_i^{\max} = \frac{E_i^{\max}}{4}, \qquad \forall i \in \mathcal{B}, \tag{3.20}$$

which corresponds to a four-hour battery system.

Constraint (3.20) ensures consistent battery sizing by fixing the ratio between inverter power and the nominal installed energy capacity. Under this formulation, the battery has a nominal duration of four hours, meaning that its rated power is one quarter of its installed energy capacity. Since battery operation is further restricted by the state-of-charge limits, only a fraction of the nominal energy capacity is available during normal operation.

Energy-installment coupling To ensure that energy capacity is only considered when a battery is installed at a given bus, a Big-M type coupling constraint is introduced between the binary placement decision variable b_i and the continuous energy capacity variable $E_i^{\max}$. This enforces that no energy storage capacity can exist at a bus unless a battery installation is selected.

$$E_i^{\max} \leq E^{\text{cap}} \cdot b_i \qquad \forall i \in \mathcal{B}. \tag{3.21}$$

The resulting formulation integrates network operation, photovoltaic generation, battery investment decisions, and battery operation within a LinDistFlow optimization framework. The following chapter applies this formulation to the selected SimBench low-voltage network and describes the case study setup, data preparation, and experimental scenarios used to evaluate the proposed approach.

4

Case Studies

To systematically assess the technical and economic impact of BESS deployment, a benchmark distribution network must first be selected that is sufficiently representative of Dutch residential LV grids while offering realistic load data. This chapter, therefore, first motivates the network choice and describes the network topology and load composition. Subsequently, the experimental scenarios and evaluation metrics used throughout the remainder of the thesis are introduced. The accompanying code can be found in the Github repository.[1]

4.1 Benchmark Network

The low-voltage network used throughout this thesis is based on the SimBench benchmark system `1-LV-semiurb4-0-sw`. SimBench[2] provides standardized electrical network models derived from real-world German grid data, including detailed component parameters, network topology, and time-series demand and generation profiles. The framework is widely adopted in power systems research because it enables reproducible experimentation and facilitates comparison across studies.

The selected network represents a semi-urban low-voltage feeder and was chosen for two primary reasons. First, its radial structure closely resembles the topology of Dutch residential low-voltage distribution networks. This is particularly suitable because the optimization model developed in this thesis is based on a linearized DistFlow (LinDistFlow) formulation, which assumes a tree-like feeder without loops.

[1] https://github.com/ThomasBredee/VU26_BA_Thesis
[2] https://simbench.de/de/datensaetze/

Second, the network exhibits representative low-voltage demand characteristics across its buses, making it suitable for investigating localized congestion phenomena and optimal battery placement decisions. Figure 4.1 visualizes the extracted 44-bus network topology used in the optimization model. Each node represents a bus, while the edges denote electrical connections between buses. The node coloring reflects the annual energy demand at each bus, where darker red nodes indicate higher-demand consumers and lighter yellow nodes correspond to lower-demand residential users.

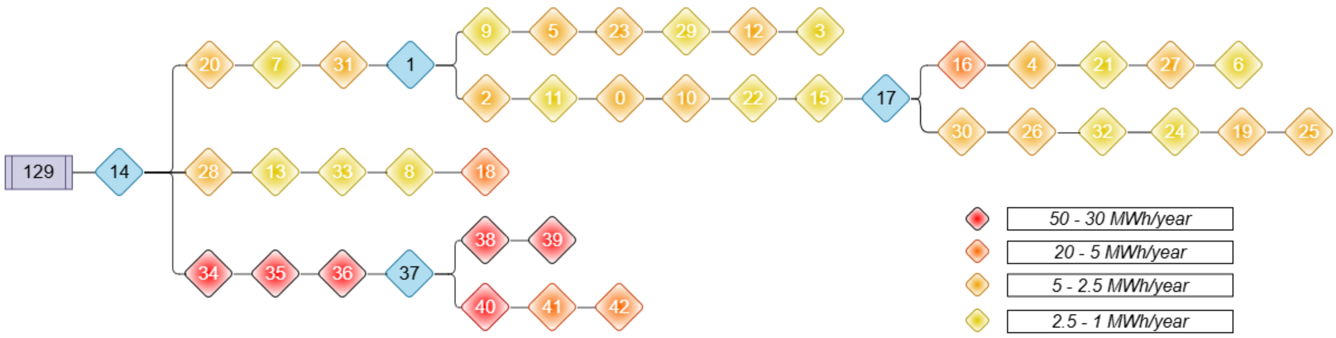

Figure 4.1: 44-bus low-voltage network topology.

The visualization highlights a clear concentration of high-demand buses in the branch of the feeder of buses 34 to 42, particularly around buses 34 through 40. These buses exhibit substantially larger annual demand values than the remainder of the network and are therefore expected to play an important role in determining voltage behavior, power flow congestion, and economically attractive battery placement locations. Bus 1, 14, 17 and 37 have no demand and serve as connection buses.

Table 4.1 summarizes the annual energy demand assigned to each bus in MWh per year. The demand values were obtained by aggregating the native SimBench load profiles over the full simulation horizon and normalizing them using the demand value coupled to that bus.

Although SimBench is based on German benchmark data, the radial structure of the selected network is comparable to Dutch low-voltage distribution systems to provide a realistic and representative case study. This makes the network an appropriate foundation for evaluating community-level BESS.

Annual Demand Range	Number of Buses	Color coding Fig 4.1
50 – 30 MWh/year	7	dark-red
20 – 5 MWh/year	9	dark-orange
5 – 2.5 MWh/year	20	light-orange
2.5 – 1 MWh/year	6	yellow

Table 4.1: Distribution of annual bus-level energy demand.

4.2 Modeling Choices

The optimization model is formulated over a one-year time horizon with an hourly resolution, resulting in 8760 time steps. This temporal granularity is chosen to capture seasonal variations in electricity demand, photovoltaic (PV) generation, and electricity prices. Such long-term variations are essential for evaluating both battery investment decisions and operational behavior.

The underlying electrical system is assumed to be radial throughout this research. This assumption is consistent with the selected low-voltage distribution network and enables the use of the LinDistFlow formulation introduced in Chapter 3.

All electrical quantities are expressed in the per-unit (p.u.) system. A system base power of 1 MVA is used as the reference for all conversions. This normalization is applied to line impedances, transformer parameters, power flows, and voltage magnitudes, ensuring a consistent representation of all electrical quantities within the optimization model.

Operational constraints are defined according to standard distribution system limits. Voltage magnitudes are restricted to the range 0.95–1.05 p.u. The slack bus voltage is fixed at 1.025 p.u., creating an asymmetric voltage margin around the operating point. Consequently, the network has 0.025 p.u. of upward voltage headroom and 0.075 p.u. of downward voltage headroom, implying that overvoltage constraints may become binding before undervoltage constraints under increasing PV penetration. Line capacity constraints are derived directly from the thermal current ratings provided in the SimBench dataset, while transformer loading is constrained through an apparent power limit.

The optimization problem is formulated as a mixed-integer linear program (MILP) and solved using Gurobi. All experiments are solved to the specified optimality tolerance described in the implementation settings. Simulation outputs are automatically exported for post-processing, enabling systematic comparison across scenarios and sensitivity analyses.

4.2.1 Demand Modeling

Electrical demand is modeled at the bus level using hourly time series over a one-year horizon. The annual energy demand associated with each bus is derived from the original SimBench load profiles. Rather than using a single network snapshot, the full 15-minute SimBench demand time series is integrated over the year to obtain the annual energy consumption at each bus:

$$E_i^D = \frac{1000\,\Delta t^{SB}}{S^{base}} \sum_{\tau} P_{i,\tau}^{SB},$$

where $P_{i,\tau}^{SB}$ denotes the SimBench active power demand at bus i and time step τ, $\Delta t^{SB} = 0.25$ h is the SimBench time resolution, and S^{base} is the system base power.

To construct hourly demand profiles, standardized Dutch residential electricity consumption profiles are used[1]. These profiles were developed in collaboration with Dutch DSOs and TSOs and are publicly provided for operational planning studies. The original quarter-hourly data is aggregated to hourly values to match the optimization time step used throughout the model.

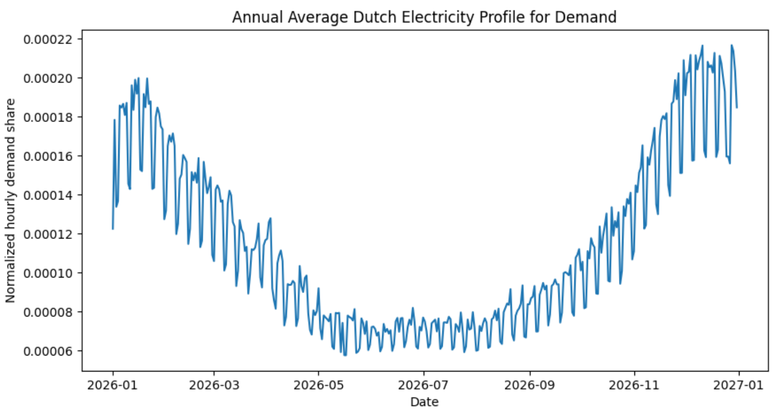

Figure 4.2: Annual normalized demand profile used within the case study.

The resulting hourly demand profile is normalized such that

$$\sum_{t \in \mathcal{T}} \rho_t^D = 1$$

where ρ_t^D represents the normalized share of annual electricity consumption occurring during hour t. The active demand at each bus is subsequently constructed as

[1]https://energiedatawijzer.nl/

$$p_{i,t}^D = E_i^D \rho_{i,t}^D, \qquad \forall i \in \mathcal{B}, \forall t \in \mathcal{T},$$

where E_i^D denotes the annual energy demand at bus i. Figure 4.2 illustrates the normalized Dutch demand profile used within the case study. The profile captures seasonal variations in electricity consumption throughout the year. Figure 4.3 presents the corresponding average daily demand pattern, showing the characteristic residential demand peaks around 08:00 and during the evening hours between 17:00 and 21:00.

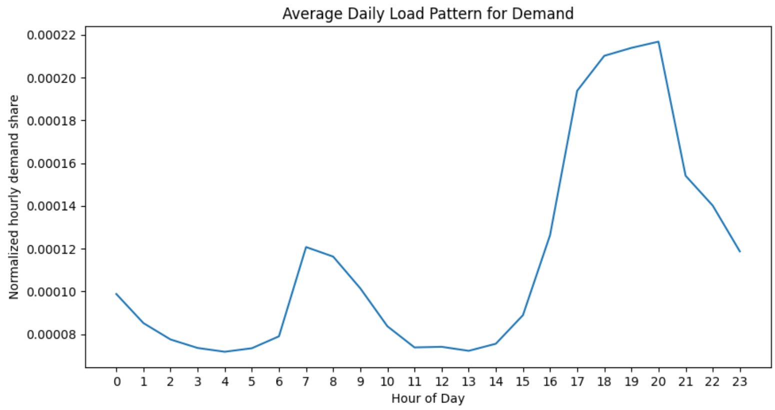

Figure 4.3: Average daily demand profile derived from the yearly demand data.

To avoid unrealistic synchronization between all buses, temporally correlated stochastic variations are introduced through an autoregressive AR(1) process. For each bus, a unique stochastic component is generated according to

$$\epsilon_{i,t} = \rho \epsilon_{i,t-1} + \sigma z_{i,t}, \tag{4.1}$$

where $z_{i,t} \sim \mathcal{N}(0,1)$, $\rho = 0.9$, and $\sigma = 0.08$. The resulting demand profile is clipped to prevent negative demand values and subsequently renormalized such that the annual energy demand E_i^D remains unchanged. Consequently, each bus exhibits a unique demand pattern while preserving its annual energy consumption.

Figure 4.4 presents three example demand profiles after the introduction of the autoregressive stochastic component, Bus 6 (blue), Bus 7 (orange), and Bus 22 (Green). All profiles correspond to the same annual energy demand but exhibit different temporal realizations due to the bus-specific stochastic variation.

Reactive power demand is not modeled independently. Instead, the reactive demand at each bus is derived from the active power demand using a bus-specific Q/P ratio extracted

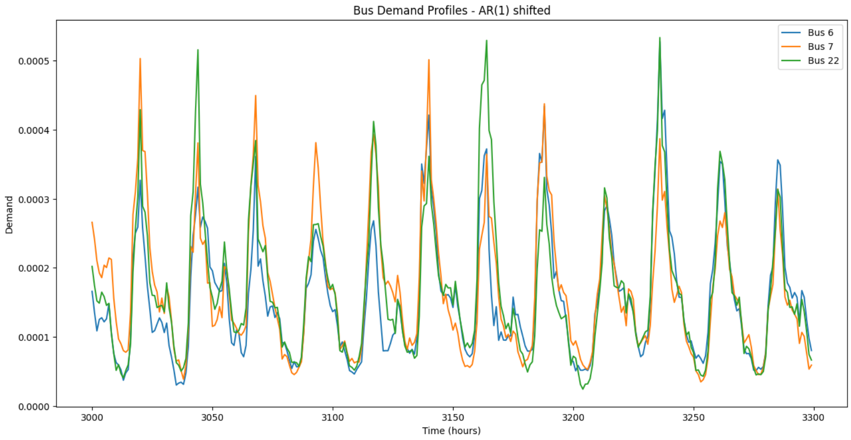

Figure 4.4: Examples of nodal demand profiles after the addition of autoregressive stochastic demand variations.

from the SimBench network data.

$$q_{i,t}^{D} = \left(\frac{Q_i}{P_i}\right) p_{i,t}^{D}.$$

Although the formulation allows this ratio to differ between buses, all loads in the selected SimBench network share the same power factor. As a result, the calculated Q/P ratio is identical for all buses and equal to 0.3952. This preserves the original power factor characteristics of the network while maintaining consistency between active and reactive power consumption over time.

4.2.2 PV Modeling

Photovoltaic (PV) generation is modeled at the bus level, where each bus may receive a certain annual PV energy budget depending on the selected PV allocation strategy. The temporal generation behavior is derived from standardized Dutch PV production profiles, which are converted to an hourly resolution. Similar to the demand modeling framework, the yearly PV profile is normalized such that:

$$\sum_{t \in \mathcal{T}} \rho_t^{PV} = 1.$$

The normalized profile, therefore, represents the temporal distribution of annual PV generation rather than an installed generation capacity.

For each bus i, an annual PV energy budget E_i^{PV} is assigned. The hourly PV generation is then constructed as

$$p_{i,t}^{PV} = E_i^{PV} \rho_t^{PV}, \qquad \forall i \in \mathcal{B}, \forall t \in \mathcal{T}, \tag{4.2}$$

where ρ_t^{PV} denotes the normalized PV production profile. Consequently, all buses follow the same temporal PV generation pattern while differing in their total annual PV production.

All reported results are obtained under the unity power factor assumption ($q_{i,t}^{PV} = 0$); the reactive support mode is implemented as an optional extension but is not used in the experiments presented in this thesis.

Also, the inverter apparent power rating is determined based on the peak PV generation at each bus. A sizing margin of 10% is included to ensure sufficient inverter headroom for reactive power support during high PV generation periods. This allows the PV systems to contribute to voltage regulation while respecting inverter apparent power limits.

Multiple PV allocation strategies are considered within the framework. The *base* strategy distributes PV proportionally across all buses according to their local annual electricity demand. In this case, buses with higher annual demand receive larger annual PV energy budgets.

4.2.2.1 PV placement: bus / voltage instability

In addition, two network-aware PV placement methodologies are implemented to investigate how concentrated PV deployment affects network performance compared to the baseline scenario of proportional PV allocation across all buses. The proportional allocation strategy serves as the primary case study, while the network-aware approaches are evaluated as sensitivity scenarios that deliberately concentrate PV generation at electrically critical locations.

These targeted placement strategies are not intended to represent realistic PV adoption patterns. Instead, they act as stress-test scenarios that examine the robustness of the network under unfavorable PV deployment conditions. Both approaches are derived from network sensitivity indicators calculated from a reference scenario without PV generation or battery storage.

The first strategy is based on a voltage severity ranking. Using the voltage profiles obtained from the reference scenario, each bus is evaluated according to the magnitude and variability of its voltage behavior over the yearly simulation horizon. For every bus, the minimum voltage, maximum voltage, average voltage, and voltage standard deviation are extracted from the exported voltage profile results.

Based on these quantities, two intermediate indicators are computed. First, the voltage spread is determined as

$$\text{spread}_i = V_i^{\max} - V_i^{\min},$$

which captures the yearly voltage variation at bus i. Second, the maximum voltage deviation from the nominal voltage is computed as

$$\text{maxDeviation}_i = \max\left(|V_i^{\min} - 1|, |V_i^{\max} - 1|\right),$$

which measures the largest deviation from the nominal voltage of 1 p.u.

It should be noted that these indicators are computed using voltage magnitudes V expressed in p.u., rather than the squared voltage variables v used within the LinDistFlow formulation. Using voltage magnitudes improves interpretability while preserving the relative ranking of voltage-sensitive buses.

Both terms are combined into a single voltage severity score:

$$\text{severityScore}_i = \text{spread}_i + \text{maxDeviation}_i.$$

The buses are subsequently ranked from highest to lowest according to this severity score. The buses with the largest voltage variations and strongest deviations receive the highest rankings. The resulting ranking is then used to allocate PV capacity preferentially to the most voltage-sensitive locations in the network. Figure 4.6 depicts the 15 buses with the highest voltage severity, where red indicates the buses with the largest voltage deviations, while orange and yellow indicate the top 10 and top 15 highest voltage-severity buses, respectively. This ranking shows that the largest voltage deviations occur at the leaf (end-of-feeder) nodes. These 15 buses, representing approximately one-third of the network, receive PV generation in an attempt to compensate for the voltage drop across the network.

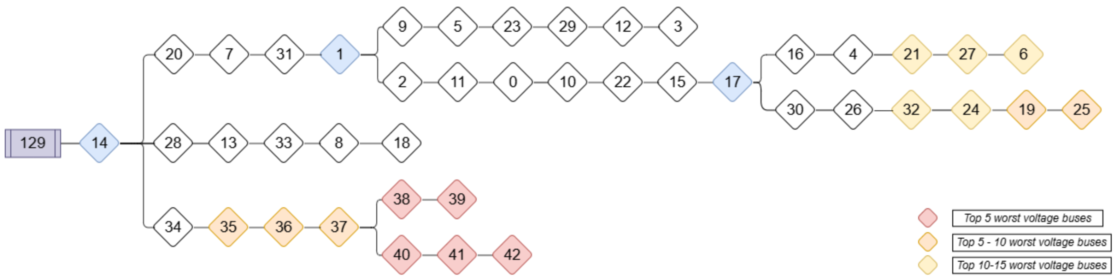

Figure 4.5: Top 15 Voltage ranking in 3 categories.

4.2.2.2 PV Placement: Network Loading Stability Index

The second network-aware PV placement strategy is based on the Network Loading Stability Index (NLSI), proposed by Khalil et al. (7). The NLSI is a line-based voltage stability indicator that combines line impedance, power flow, and local voltage conditions into a single measure of electrical stress. For each line segment (i, j) and time period t, the index is calculated as

$$\mathrm{NLSI}_{ij,t} = \frac{R_{ij}P_{ij,t} + X_{ij}Q_{ij,t}}{0.25V_{i,t}^2},$$

where R_{ij} and X_{ij} denote the line resistance and reactance, $P_{ij,t}$ and $Q_{ij,t}$ represent the active and reactive power flows, and $V_{i,t}$ is the sending-end voltage magnitude. Values approaching one indicate that the line operates closer to its voltage stability limit.

In the original methodology, the NLSI is used to identify weak network locations and reduce the search space for distributed generation placement. Rather than employing the index within a metaheuristic optimization framework, this study uses the NLSI as a deterministic ranking criterion for PV allocation. The index is evaluated for every line over the full simulation horizon of the reference network without PV generation or battery storage.

Since the NLSI is defined at the line level, each line score is assigned to its receiving bus. Furthermore, absolute active and reactive power flows are used, such that the metric captures the magnitude of electrical stress independent of flow direction. For each bus, the maximum NLSI value observed during the year is retained:

$$\mathrm{NLSI}_i^{\max} = \max_t \left(\mathrm{NLSI}_{ij,t}\right).$$

The buses are subsequently ranked according to $\mathrm{NLSI}_i^{\max}$, and the fifteen highest-ranked buses are selected as the candidate locations for concentrated PV deployment. This placement strategy represents a stress-test scenario in which PV generation is intentionally allocated to electrically sensitive areas of the network.

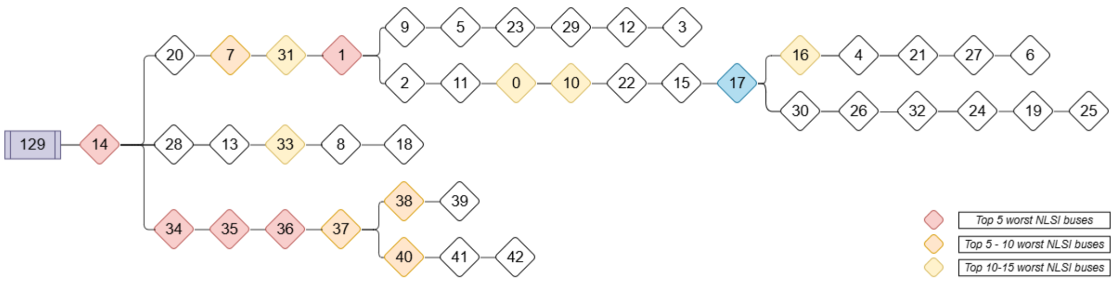

Figure 4.6: Top 15 NLSI ranking buses in 3 categories.

4.2.2.3 Final PV placement weight

To avoid unrealistically concentrating PV installations on a small number of electrically weak but low-demand buses, a hybrid allocation metric is introduced. The placement strategy combines both electrical vulnerability and local annual electricity demand into a single weighted score.

First, the top-15 most critical buses are selected based on either the voltage severity ranking or the line stability ranking. Subsequently, a hybrid score is computed for each selected bus using a logarithmically scaled vulnerability metric combined with the local demand magnitude. The logarithmic transformation prevents a single extreme bus from dominating the allocation, while still prioritizing electrically sensitive locations.

The hybrid score is defined as:

$$H_i = [\log(1 + S_i)^{\alpha}] \cdot D_i^{\beta}$$

where: H_i denotes the hybrid allocation score for bus i, S_i represents the electrical severity indicator, D_i denotes the annual electricity demand at bus i, $\alpha = 0.7$ controls the importance of electrical severity, $\beta = 0.3$ controls the contribution of local demand.

The resulting hybrid scores are subsequently normalized to determine the final PV allocation weights:

$$w_i = \frac{H_i}{\sum_{j \in \mathcal{B}} H_j}$$

where w_i represents the fraction of the total PV budget allocated to bus i.

This approach creates a smoother and more realistic alternative PV deployment strategy by balancing electrical network vulnerability with spatial demand characteristics, while avoiding excessive concentration of PV capacity at a limited number of buses. Table 4.2 presents the resulting hybrid allocation weights for the top-15 buses ranked according to the voltage severity metric. Similarly, Table 4.3 shows the hybrid PV allocation based on the NLSI. The decision was made, as clear from the two tables, that no PV could be allocated to the nodes 1, 14, 17 or 37 because these buses do not have an aboveground connection nor do they have any physical space to place the solar panels.

Rank	**Bus**	**Severity Score**	**Demand [MWh/year]**	**Hybrid Score**	**Weight**
1	42	0.0691	11.892	0.316	0.075
2	39	0.0689	46.007	0.474	0.112
3	41	0.0688	19.568	0.366	0.087
4	38	0.0684	32.878	0.426	0.101
5	40	0.0683	49.473	0.481	0.114
6	37	0.0665	0.000	0.000	0.000
7	36	0.0643	30.914	0.401	0.095
8	25	0.0601	4.653	0.217	0.051
9	19	0.0597	4.888	0.219	0.052
10	35	0.0597	42.173	0.419	0.099
11	24	0.0596	2.444	0.178	0.042
12	32	0.0590	1.984	0.166	0.039
13	6	0.0590	2.444	0.177	0.042
14	27	0.0590	3.666	0.200	0.047
15	21	0.0589	2.327	0.174	0.041

Table 4.2: Hybrid PV allocation weights for the voltage-severity-based placement scenario.

Rank	**Bus**	**NLSI$_{max}$**	**Demand [MWh/year]**	**Hybrid Score**	**Weight**
1	14	0.0791	0.000	0.000	0.000
2	34	0.0409	47.776	0.335	0.308
3	36	0.0186	30.914	0.171	0.157
4	35	0.0157	42.173	0.167	0.153
5	1	0.0093	0.000	0.000	0.000
6	37	0.0091	0.000	0.000	0.000
7	7	0.0090	2.444	0.048	0.044
8	38	0.0077	32.878	0.094	0.086
9	40	0.0074	49.473	0.104	0.096
10	17	0.0054	0.000	0.000	0.000
11	10	0.0052	3.666	0.037	0.034
12	31	0.0050	3.102	0.035	0.032
13	33	0.0049	1.833	0.029	0.026
14	0	0.0044	3.102	0.031	0.029
15	16	0.0040	7.332	0.038	0.035

Table 4.3: Hybrid PV allocation weights for the NLSI-based placement scenario.

4.2.3 Electricity Price Modeling

Electricity prices are modeled using historical Dutch day-ahead market prices for the year 2025[1]. These prices are used to represent the temporal variation in electricity procurement costs faced by the distribution network throughout the simulation horizon. The electricity price profile shows temporal variability over the year, including both high-price periods and occasional negative-prices. For visibility, Figure 4.7 illustrates the hourly electricity prices during the first half of 2025, while the full profile is available in the Appendix. Large fluctuations can be observed between periods of low and high electricity prices, which create arbitrage opportunities for the model to optimize the storage of energy.

The battery systems are economically incentivized to charge during periods with low electricity prices and discharge during periods with high electricity prices. In this way, the optimization model captures the economic value of temporal energy shifting.

Curtailment costs are linked directly to the electricity market price. During positive-price periods, curtailed photovoltaic energy receives a penalty equal to the market value

[1]Downloaded from https://wattsmart.app/electricity-prices/netherlands/, a visualization tool based on the original ENTSO-E Transparency Platform data available at https://transparency.entsoe.eu/.

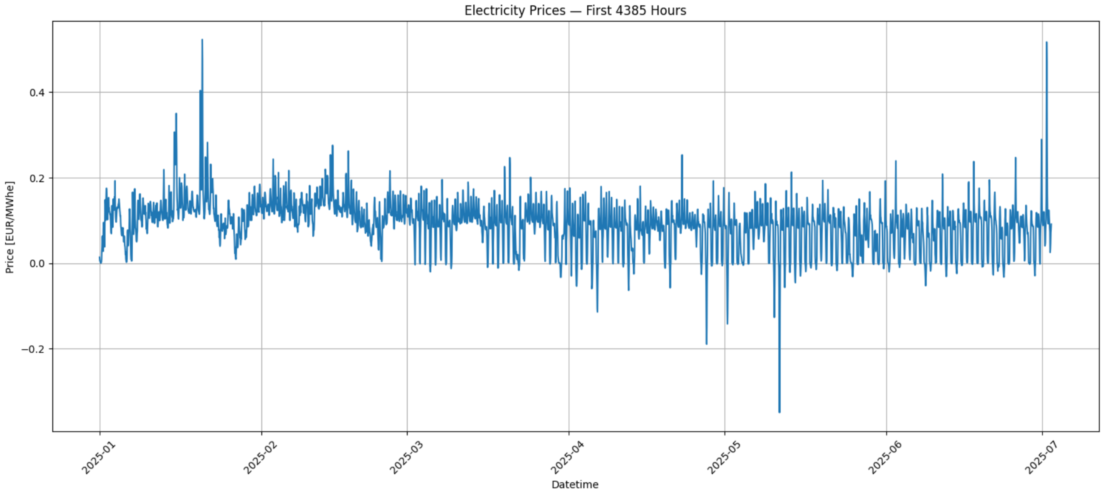

Figure 4.7: Hourly Dutch day-ahead electricity prices during the first half of 2025.

of the lost electricity. During negative-price periods, the curtailment penalty is set equal to zero. This reflects the assumption that avoiding electricity export during negative-price conditions does not result in an additional economic loss.

To further illustrate the seasonal behavior of electricity prices, Figure 4.8 compares the average daily price patterns during summer and winter periods. The winter period generally exhibits higher electricity price peaks compared to the summer period. Additionally, due to the transition between Dutch summer time and winter time, the timing of the daily peaks is shifted by approximately one hour.

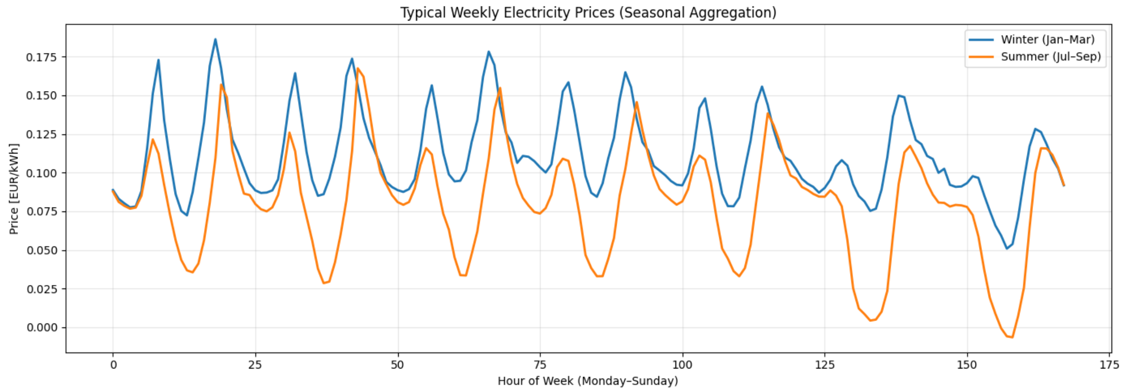

Figure 4.8: Average daily electricity price patterns during summer and winter periods.

4.2.4 Battery Energy Storage System (BESS) Modelling

Battery Energy Storage Systems (BESS) are modeled as flexible distributed assets that can be installed at selected buses throughout the distribution network. The optimization model determines both the optimal placement and sizing of the battery systems, while simultaneously optimizing their charging and discharging schedules over the considered time horizon. This allows energy to be stored and shifted in time in response to network conditions and electricity prices.

To preserve battery lifetime and avoid excessive charging or discharging, the state of charge is constrained within predefined operating limits. The minimum and maximum state-of-charge are denoted by σ_{min} and σ_{max}, respectively. The battery energy level must remain within these bounds throughout the optimization horizon.

Parameter	Symbol	Value	Unit
Power investment cost	c^P	360	EUR/kW
Energy investment cost	c^E	210	EUR/kWh
Discount rate	r	0.05	–
Battery lifetime	L	10	years
Cycle lifetime	N_{cycles}	5000	cycles
Round-trip efficiency	η^{rt}	0.95	–
Minimum state-of-charge	σ_{min}	0.10	–
Maximum state-of-charge	σ_{max}	0.90	–

Table 4.4: Battery Energy Storage System parameters used throughout the optimization model.

Battery investment costs are represented using separate power-related and energy-related capital cost components. The main BESS assumptions used throughout this research are summarized in Table 4.4. These values are used both in the investment formulation and in the operational battery model.

To incorporate long-term investment decisions into the annual operational optimization problem, battery investment costs are annualized using a Capital Recovery Factor (CRF). A discount rate of $r = 5\%$ and an assumed battery lifetime of $L = 10$ years are used, resulting in

$$\alpha = \frac{r(1+r)^L}{(1+r)^L - 1} \approx 0.1295.$$

The battery systems are modelled with a round-trip efficiency of 95%. Charging and discharging efficiencies are assumed to be symmetric and are therefore implemented as

$$\eta = \sqrt{\eta^{rt}},$$

where η^{rt} denotes the round-trip efficiency.

In addition to investment costs, battery degradation costs are incorporated through a throughput-dependent penalty term. The degradation cost coefficient is derived from the battery energy investment cost and the assumed cycle lifetime of the battery. A cycle lifetime of 5000 full cycles is assumed, resulting in

$$c^{deg} = \frac{c^E}{2N_{\text{cycles}}} \approx 0.021 \text{ EUR/kWh},$$

where N_{cycles} denotes the number of full charge-discharge cycles. This formulation assumes that a full cycle corresponds to approximately twice the battery energy capacity in cumulative energy throughput and therefore provides a linear approximation of battery ageing.

The optimization model does not impose a fixed initial state of charge. Instead, the initial battery energy level is treated as a decision variable, subject to the state-of-charge limits. To ensure a cyclic yearly operation, the battery energy level at the final time step is constrained to equal the energy level at the first time step.

A maximum nominal battery energy capacity is imposed through the parameter E^{cap}. This value is chosen to equal four hours of the transformer apparent power rating:

$$E^{\text{cap}} = 4 \cdot S^{\text{trafo}}.$$

The battery energy variable $E_i^{\max}$ therefore represents the *nominal* installed energy capacity. Since the operational energy level is constrained by the state-of-charge window $[0.10, 0.90]$, only a fraction $(0.90 - 0.10)E_i^{\max}$ is available for charging and discharging.

No minimum battery size is imposed in the optimization model. This allows the model to determine the economically optimal battery capacity without introducing an artificial lower bound. Imposing a minimum size could bias the solution by forcing battery installations that are not justified by the operational and economic conditions of the network.

4.3 Case Study Designs

The case studies are structured around three sub-questions, each targeting a different aspect of technical performance, model sensitivity, and operational behavior.

4.3.1 Experiment 1: Battery Siting Performance

This case study investigates how the installation of different numbers of BESS affects the performance of the distribution network. The purpose of this case study is twofold. First, it evaluates the technical benefits of installing batteries within the network. Second, it examines the siting decisions made by the optimization model, including where batteries are placed and how much storage capacity is installed at each location in comparison to the local (and surrounding) demand. This case study aims to answer the research question:

> *Where does the model place BESS and how does the installation of a different number of BESS affect voltage violations, network congestion, and investment decisions under different scenarios?*

This section evaluates the battery placement decisions of the optimization model under different system development scenarios. Two main scenario families are considered. Scenario S1 corresponds to the baseline network with PV = 1.0 and electrification = 1.0. Scenario S2 represents a future development case with increased PV penetration (1.5). In both cases, the maximum number of batteries is varied between one and ten. The resulting experiments are denoted as S1.B0–B10 and S2.B0–B10 respectively.

For each scenario, the optimization model determines both the battery locations and battery sizes that minimize total system costs while satisfying all network constraints. The resulting scenarios allow the impact of battery deployment on network performance to be evaluated under both present-day and more demanding future operating conditions. The 22 different experiments are summarized in Table 4.5.

Scenario	PV Penetration	Electrification	Allowed BESS
S1.B[0-10]	1.0	1.0	{0,1,2, ..., 9,10}
S2.B[0-10]	1.5	1.0	{0,1,2, ..., 9,10}

Table 4.5: Testing matrix for the battery siting performance case study.

Secondly, a third set of experiments (S3) considers joint growth of electricity demand and photovoltaic generation. The electrification factor is used to scale the annual electricity demand, while the PV penetration factor is increased in parallel. This represents a future scenario where higher electricity consumption due to electrification is accompanied by increased distributed PV adoption.

Seven levels of future development are evaluated. The electrification factor ranges from 1.0 to 2.5, while the PV penetration factor ranges from 1.0 to 1.75. For each development level, the maximum number of batteries that may be installed is set to zero, one, or two. By simultaneously increasing demand and PV generation, this experiment evaluates how the economic and technical value of battery storage changes under increasingly demanding future operating conditions. In total, 21 experiments are performed, summarized in Table 4.6. The instance in scenario have unique identifiers, which are defined as S3.EX.BY, where $X \in \{100, 125, 150, 175, 200, 225, 250\}$ and $Y \in \{0, 1, 2\}$.

Scenario	PV Penetration	Electrification	Allowed BESS
S3.E100.B[0-2]	1.000	1.00	{0,1,2}
S3.E125.B[0-2]	1.125	1.25	{0,1,2}
S3.E150.B[0-2]	1.250	1.50	{0,1,2}
S3.E175.B[0-2]	1.375	1.75	{0,1,2}
S3.E200.B[0-2]	1.500	2.00	{0,1,2}
S3.E225.B[0-2]	1.625	2.25	{0,1,2}
S3.E250.B[0-2]	1.750	2.50	{0,1,2}

Table 4.6: Testing matrix of battery placement in heightened electrification scenarios.

4.3.2 Experiment 2: PV Sensitivity Analysis

The second experiment investigates how assumptions regarding the spatial distribution of photovoltaic (PV) generation influence optimal battery investment decisions. While the previous experiments focused on increasing electrification, this experiment isolates the impact of PV deployment by evaluating multiple PV allocation strategies under increasing PV penetration levels. The objective is to determine whether different PV deployment patterns result in different battery placement and sizing, answering the research sub-question:

> *How sensitive is optimal BESS sizing and placement to different photovoltaic deployment assumptions, such as PV placement strategies?*

Three PV allocation strategies are considered:

1. **Proportional allocation.** PV generation is distributed proportionally across all buses according to their annual electricity demand, representing a demand-proportional adoption of rooftop PV throughout the network.

2. **Voltage Severity allocation (Bus).** PV generation is concentrated at electrically weak buses identified through the voltage severity ranking described in Section 4.2.2.

3. **Line Stability allocation (Line).** PV generation is concentrated at buses connected to electrically critical feeder sections identified using the Network Loading Stability Index (NLSI).

The last two allocation strategies represent stress-test scenarios that intentionally concentrate PV generation at electrically sensitive locations. They are not intended to predict future PV adoption, but to evaluate whether alternative deployment patterns influence battery planning decisions.

For each PV allocation strategy, the annual PV energy budget is varied between 100% and 200% of the annual network demand in increments of 25%. Unlike Experiment 1, the electrification factor remains fixed at 1.00 to isolate the impact of increasing PV penetration. For every scenario, the optimization is repeated while allowing zero, one, or two Battery Energy Storage Systems (BESS), enabling the model to determine their optimal placement and sizing.

Table 4.7 summarizes the complete experimental design.

Scenario ID	**PV Allocation Strategy**	**PV Factor**	**Electrification Factor**	**Allowed BESS**
S4.Prop.PV100	Proportional	1.00	1.00	{0,1,2}
S4.Prop.PV125	Proportional	1.25	1.00	{0,1,2}
S4.Prop.PV150	Proportional	1.50	1.00	{0,1,2}
S4.Prop.PV175	Proportional	1.75	1.00	{0,1,2}
S4.Prop.PV200	Proportional	2.00	1.00	{0,1,2}
S4.Bus.PV100	Voltage Severity (Bus)	1.00	1.00	{0,1,2}
S4.Bus.PV125	Voltage Severity (Bus)	1.25	1.00	{0,1,2}
S4.Bus.PV150	Voltage Severity (Bus)	1.50	1.00	{0,1,2}
S4.Bus.PV175	Voltage Severity (Bus)	1.75	1.00	{0,1,2}
S4.Bus.PV200	Voltage Severity (Bus)	2.00	1.00	{0,1,2}
S4.Line.PV100	Line Stability (NLSI)	1.00	1.00	{0,1,2}
S4.Line.PV125	Line Stability (NLSI)	1.25	1.00	{0,1,2}
S4.Line.PV150	Line Stability (NLSI)	1.50	1.00	{0,1,2}
S4.Line.PV175	Line Stability (NLSI)	1.75	1.00	{0,1,2}
S4.Line.PV200	Line Stability (NLSI)	2.00	1.00	{0,1,2}

Table 4.7: Scenario matrix for the PV sensitivity analysis.

4.3.3 Experiment 3: Electricity Market Sensitivity Analysis

The previous experiments focus on the technical performance of batteries under different levels of electrification and PV penetration. This analysis identifies optimal battery locations, capacities, and operational schedules from a network perspective. However, the economic value of these technically optimal solutions remains dependent on the electricity market conditions under which they operate.

Over the past decade, Dutch electricity markets have experienced substantial changes in both average price levels and price volatility. In particular, the period following 2020 has been characterized by significantly larger price fluctuations, creating additional opportunities for energy arbitrage and storage technologies. Consequently, a battery configuration that is economically unattractive under one market environment may become financially beneficial under another. To evaluate the robustness of the obtained results, a sensitivity analysis is performed in which the technical decisions determined by the optimization model are held fixed, while the electricity price profile used for economic evaluation is varied.

This experiment addresses the following research question:

> *How sensitive are the economic benefits of optimally sized and placed BESS installations to different historical electricity market conditions?*

Unlike the previous experiments, no additional optimization runs are performed. Instead, the battery placement, sizing, charging schedules, discharging schedules, and PV curtailment decisions obtained from the optimization model are reused. The objective function is subsequently recalculated using historical Dutch day-ahead electricity prices from different years. This approach isolates the influence of electricity market conditions from the technical characteristics of the network and battery system.

Given that the objective of this experiment is to evaluate the economic value of battery storage under different price environments, a single representative scenario is selected. The baseline electrification scenario from Experiment 1 is used, comparing the case without battery storage (S3.E100.B0) against the corresponding case with two batteries (S3.E100.B2). This scenario was chosen because it represents the least congested network configuration while still allowing the operational benefits of battery storage to be evaluated. Furthermore, it avoids introducing additional effects associated with extreme electrification or PV penetration levels, thereby allowing the impact of electricity market conditions to be assessed more clearly.

Table 4.8: Electricity market sensitivity analysis scenario matrix

Scenario ID	Electrification	PV Factor	BESS	Price Years
S5.E100.B0	1.00	1.00	0	2015–2025
S5.E100.B2	1.00	1.00	2	2015–2025

The resulting scenario matrix is presented in Table 4.8.

For each scenario, the annual objective value is recalculated using historical Dutch day-ahead electricity price profiles between 2015 and 2025. All technical decisions remain unchanged, ensuring that any differences in the resulting costs are solely attributable to changes in the electricity market environment.

The selected period includes years characterized by relatively stable electricity prices as well as years exhibiting extreme price volatility. As a result, this experiment provides insight into whether the economic attractiveness of battery storage is primarily driven by the technical characteristics of the distribution network or by external electricity market conditions.

5

Evaluation

This chapter presents the results obtained from the proposed optimization model. First, the baseline network behavior without battery storage is analyzed, after which the effects of battery placement, sizing, operation, and economics are evaluated under different electrification, photovoltaic deployment, and cost scenarios.

5.1 Baseline Network Behavior Without Battery Storage

Before analyzing the battery placement and sizing decisions of the optimization model, it is useful to first identify the locations within the network that are most susceptible to voltage and loading issues in the absence of battery storage, thereby providing additional context for the subsequent analysis.

To identify the structurally weakest parts of the network, four battery-free baseline scenarios are analyzed. These scenarios correspond to the highest stress levels considered within each experiment. For the electrification analysis, the scenario with an electrification factor of 1.25 and no battery storage is selected. For the PV sensitivity analysis, the scenarios with a PV factor of 2.00 and no battery storage are considered for each of the three PV placement strategies: Proportional, Bus-based, and Line-based deployment. Together, these scenarios represent the most demanding operating conditions evaluated throughout this study.

Table 5.1 presents the ranking of buses based on their voltage behavior across the four baseline scenarios. The results show a consistent pattern, where nine of the ten highest-ranked buses appear in all four scenarios, while buses 34–42 consistently form the most critical section of the feeder. Bus 39 is identified as the weakest bus in every scenario.

Despite this consistency, the observed voltage levels remain well within the permitted operating range. The average P1 voltage of the most critical buses remains above 0.99 p.u., while the average P99 voltage remains below the upper voltage limit of 1.05 p.u. Consequently, none of the analyzed scenarios exhibit voltage violations. Although a small group of buses consistently experiences the lowest voltage levels, voltage constraints do not appear to be the primary limiting factor within the studied network.

Rank	**Electrification**	**PV Placement Strategy**			**Common**	**Avg. P1**	**Avg. P99**
		Proportional	**Bus**	**Line**			
1	39	39	39	39	39 (4/4)	0.9895	1.0254
2	38	38	42	38	38 (3/4)	0.9900	1.0253
3	42	42	38	42	42 (3/4)	0.9902	1.0251
4	41	41	41	41	41 (4/4)	0.9905	1.0250
5	40	40	40	40	40 (4/4)	0.9908	1.0250
6	37	37	37	37	37 (4/4)	0.9919	1.0247
7	36	36	36	36	36 (4/4)	0.9940	1.0244
8	35	35	35	35	35 (4/4)	0.9980	1.0243
9	34	34	34	34	34 (4/4)	1.0018	1.0244
10	25	25	25	6	25 (3/4)	1.0066	1.0272
Identical buses in Top-10					9/10	–	–
Identical buses in Top-9					9/9	–	–

Table 5.1: Comparison of voltage-based bus rankings across all baseline scenarios without battery storage.

Table 5.2: Comparison of the ten most critical lines across all baseline scenarios without battery storage. The ranking remains identical across all scenarios.

Rank	**From**	**To**	**P99 Loading (%)**				**Max Loading (%)**	**Case**
			Elec.	**Proportional**	**Bus**	**Line**		
1	14	34	75.22	60.16	60.16	60.16	99.49	Elec.
2	34	35	62.75	50.18	50.18	50.19	78.83	Elec.
3	35	36	51.67	41.32	41.31	41.33	68.70	Elec.
4	129	14	48.62	38.88	38.88	38.88	61.23	Elec.
5	36	37	43.07	34.44	34.44	34.46	55.69	Elec.
6	14	20	22.92	18.33	18.38	18.33	27.09	Elec.
7	37	40	22.08	17.66	17.66	17.67	29.74	Elec.
8	20	7	21.86	17.48	17.56	17.48	25.65	Elec.
9	37	38	21.44	17.16	17.18	17.16	27.61	Elec.
10	7	31	21.25	16.99	17.07	17.00	25.06	Elec.

A different picture emerges from the line loading analysis shown in Table 5.2. In contrast to the voltage rankings, the ranking of the ten most heavily loaded lines is identical across all four baseline scenarios. The feeder section connecting buses 14, 34, 35, 36 and 37 consistently dominates the loading rankings, indicating the presence of a persistent structural bottleneck within the network.

In particular, line 14→34 is identified as the most critical line in every scenario. This line exhibits a P99 loading between 60.2% and 75.2%, while reaching a maximum observed loading of 99.5% in the electrification scenario.

These findings indicate that any effective battery placement strategy should reduce power flows through the feeder section downstream of bus 14, enabling higher electrification. The following section therefore investigates how the optimization model responds to these network characteristics through battery placement, sizing, and operational decisions.

5.2 Battery Placement and Network Impact

The objective of this section is to evaluate how the optimization model responds when batteries are available, relative to the no-battery baseline. First, the battery siting performance is analyzed to determine whether consistent placement patterns emerge across the considered scenarios. Next, the objective function is decomposed into its individual cost components to understand the economic drivers behind the optimization decisions. Finally, the technical impact of battery deployment is evaluated through a detailed analysis of voltage profiles and line loadings.

5.2.1 Battery Siting and Sizing Evaluation

This section evaluates the battery siting decisions of the optimization model under different system scenarios. Two main scenario families are considered. Scenario S1 corresponds to the baseline network with PV = 1.0 and electrification = 1.0. Scenario S2 represents a future development case with increased PV penetration (1.5). In both cases, the maximum number of batteries is varied between one and ten. The resulting experiments are denoted as S1.B0–B10 and S2.B0–B10 respectively.

A first observation is that the optimization model does not always utilize all available battery installation locations. Although additional batteries are allowed in many scenarios, the model frequently concentrates the available storage capacity in only a small number of locations. This indicates that, from the model's perspective, distributing the storage capacity over a larger number of batteries does not necessarily provide additional economic or technical benefits.

Furthermore, both scenarios reveal a relatively consistent total installed battery capacity. In Scenario 1, the total installed battery energy remains 101.8 kWh across all experiments. Similarly, in Scenario 2, the total installed battery energy remains approximately 265.8 kWh regardless of the maximum number of batteries that may be installed. The optimization model therefore appears to identify an economically optimal total storage capacity and subsequently decides how this capacity should be distributed across the network.

To further investigate this allocation behavior, Table 5.3 and Table 5.4 summarize the battery placement results for Scenario S1 and S2 respectively. In S1, the placement is relatively distributed over the network. This is further supported by Figure 5.1, which presents a heatmap showing how frequently each bus is selected across the different variants of Scenario 1. The figure demonstrates that battery placements are spread over a relatively large number of buses, and while certain buses are selected more frequently than others, no single location consistently dominates all experiments.

S1: Max. BESS	Battery Locations	Energy [kWh]
1	24	101.8
2	3, 39	29.9, 72.0
3	19	101.8
4	4, 11, 14, 40	23.3, 16.1, 18.6, 43.7
5	1, 28	20.8, 81.0
6	0, 1, 4, 19, 28, 33	16.2, 13.9, 16.9, 11.8, 17.6, 25.4
7	15	101.8
8	25	101.8
9	0, 2, 3, 4, 5, 13, 15, 19	15.1, 4.8, 15.2, 10.0, 17.8, 17.1, 7.0, 15.1
10	0, 1, 4, 9, 11, 16, 25, 28	15.4, 13.5, 8.2, 15.4, 11.6, 9.3, 14.2, 14.3

Table 5.3: Battery placement results for Scenario S1 (PV = 1.0, Electrification = 1.0).

In contrast, a different behavior is observed in Scenario S2. As shown in Table 5.4, the optimization model repeatedly selects only a single dominant battery location, despite being allowed to install multiple batteries. In almost all experiments, the storage capacity is concentrated at buses 34, 39, or 40. These buses correspond to the largest consumers in the network and each exhibits an annual demand exceeding 45 MWh. This suggests that under higher loading conditions, the optimization model prioritizes locations with the greatest demand and strongest local peaks, concentrating the available storage capacity where it can provide the largest system-wide benefit.

S2: Max. BESS	Battery Locations	Energy [kWh]
1	40	265.8
2	39	265.8
3	39	265.8
4	34	265.8
5	39	265.8
6	39	265.8
7	34	265.8
8	39	265.8
9	39	265.8
10	40	265.8

Table 5.4: Battery placement results for Scenario S2 (PV = 1.5, Electrification = 1.0).

The results of Scenarios 1 and 2 correspond to less congested network conditions than the baseline stress scenarios analyzed in Section 5.1. Line loadings remain well below critical

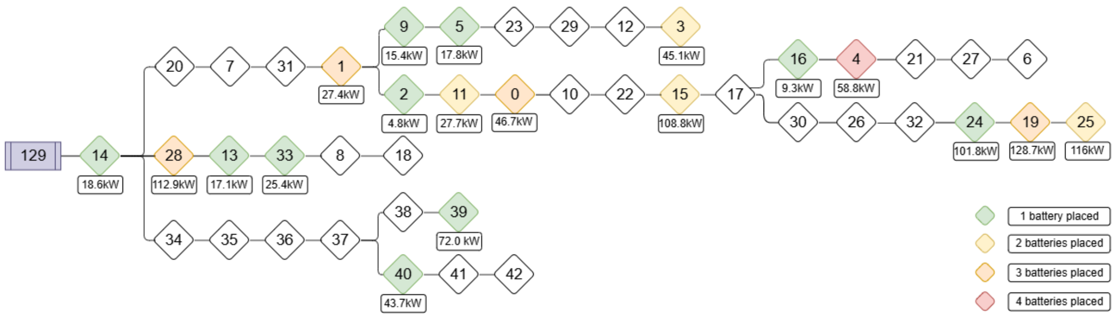

Figure 5.1: Battery placement heatmap under Scenario 1.

levels and no voltage violations are observed throughout the network. As a result, the optimization model is unable to identify clearly superior battery locations, since multiple placements provide similar benefits. Consequently, no consistent battery placement pattern emerges across these scenarios. Therefore, a third scenario with increasing electrification and PV generation is introduced under the PV placement everywhere strategy.

The results of the different battery installation and electrification scenarios S3.EX.BY are presented in Table 5.5. Because no batteries are installed in the S3.EX.B0 scenarios, these cases are omitted from the battery placement table. The scenarios S1 and S2 demonstrated that the optimization model reaches the available investment budget after installing a single battery. Allowing additional batteries therefore does not increase the total installed storage capacity, but rather redistributes the available capacity across multiple locations. For this reason, the S3 analysis is limited to a maximum of two batteries.

Table 5.5 shows the optimal battery locations and corresponding energy and power capacities for increasing levels of electrification and PV penetration. At lower electrification levels, the model installs a single battery, except for the S3.E100.B2 case. For electrification factors of 1.75 and 2.00, the model consistently selects Bus 39 and increases the battery size to 294.11 kWh and 487.26 kWh respectively.

S3.E.B	Bus	Energy [kWh]	Power [kW]
S3.E100.B1	24	101.83	25.46
S3.E100.B2	3	29.85	7.46
	39	71.98	18.00
S3.E125.B1	26	147.61	36.90
S3.E125.B2	23	147.61	36.90
S3.E150.B1	41	206.42	51.61
S3.E150.B2	39	206.42	51.61
S3.E175.B1	39	294.11	73.53
S3.E175.B2	39	294.11	73.53
S3.E200.B1	39	487.26	121.81
S3.E200.B2	39	487.26	121.81
S3.E225.B1	38	724.51	181.13
S3.E225.B2	34	405.10	101.28
	41	319.41	79.85
S3.E250.B1	37	1029.77	257.44
S3.E250.B2	34	475.43	118.86
	38	554.34	138.58

Table 5.5: Battery placement and sizing results for the S3 scenarios, ordered by electrification factor and grouped by the number of allowed batteries.

An interesting observation is that allowing two batteries rarely results in two meaningful battery installations. For electrification levels between 1.25 and 2.00, the model allocates the complete storage capacity to a single location while assigning a second battery with zero energy and power capacity. This indicates that, under these conditions, a single installation provides the most cost-effective solution. Only at the highest electrification levels of 2.25 and 2.50 does the optimization model split the available storage capacity over multiple buses, where the model selects end-of-leaf buses.

For battery sizing, Table 5.5 shows two consistent trends. First, the optimal battery power rating remains exactly one quarter of the installed energy capacity across all scenarios. This follows directly from the imposed design constraint $P_{\max} \leq E_{\max}/4$, indicating that the optimization consistently utilizes the full allowable power capability of the installed batteries.

Second, battery capacity increases more than proportionally with the electrification factor. Increasing electrification not only raises the total energy that must be shifted, but also amplifies peak demand and network congestion during critical periods. Consequently, the optimization responds with increasingly larger battery systems to provide sufficient charging and discharging power during these peak loading events, resulting in accelerated growth of both energy and power capacity as electrification increases.

5.2.2 Objective Breakdown Results

The battery placement results presented in the previous section demonstrate where, and how much, storage is installed under increasing network stress. However, they do not explain why these investments are economically justified. To better understand the drivers behind the optimization decisions, the objective function is decomposed into its individual cost components. This allows the relative contributions of energy procurement, battery investment, battery degradation, and PV curtailment costs to be evaluated across different electrification and PV penetration levels. Furthermore, the analysis provides insight into whether batteries are primarily installed to reduce operational costs or to maintain network feasibility under increasingly constrained operating conditions.

Table 5.6 presents the objective value decomposition for all solved instances of Scenario 3. Figure 5.2 visualizes the same results. A clear trend can be observed across all scenarios: increasing electrification leads to substantially higher total system costs. This increase is driven by three factors. First, higher electricity demand results in increased energy procurement costs. Second, larger battery installations are required to maintain network feasibility, leading to higher investment costs. Third, PV curtailment costs increase with PV penetration because the network is unable to utilize all available photovoltaic generation, resulting in higher levels of curtailed energy.

For the case without batteries, feasible solutions are obtained only up to an electrification factor of 1.25. The total system cost increases from €43,808 at the baseline scenario to €56,495 at an electrification factor of 1.25. Beyond this point, no feasible solution could be obtained without storage, indicating that the network is unable to accommodate further growth in demand and PV generation while satisfying all operational constraints.

The introduction of battery storage significantly extends the feasible operating range of the network. While the network without storage remains feasible only up to an electrification factor of 1.25, the availability of either one or two batteries enables feasible operation for all investigated scenarios up to an electrification factor of 2.50. As network stress increases, the optimization model responds by installing progressively larger batteries, causing annualized investment costs to increase from approximately €3,956 in the baseline scenario to more than €40,000 in the most extreme scenario. Battery degradation costs follow a similar trend, reflecting the increased energy throughput of larger storage systems.

A more detailed examination of the objective components reveals that the growth in battery capacity is not solely driven by congestion management requirements. Higher

BESS	Elec.	PV	Total [€]	Energy [€]	Invest. [€]	Degrad. [€]	Curtail. [€]
0	1.00	1.00	43,808	33,454	0	0	10,354
1	1.00	1.00	43,442	29,756	3,956	1,336	8,393
2	1.00	1.00	43,442	29,756	3,956	1,336	8,393
0	1.25	1.12	56,495	41,341	0	0	15,153
1	1.25	1.12	55,836	35,973	5,735	1,944	12,184
2	1.25	1.12	55,836	35,973	5,735	1,944	12,184
1	1.50	1.25	68,929	41,593	8,020	2,717	16,599
2	1.50	1.25	68,929	41,593	8,020	2,717	16,599
1	1.75	1.38	82,763	46,111	11,427	3,845	21,381
2	1.75	1.38	82,763	46,111	11,427	3,845	21,381
1	2.00	1.50	97,703	47,238	18,931	6,194	25,341
2	2.00	1.50	97,703	47,238	18,931	6,194	25,341
1	2.25	1.62	114,198	47,558	28,148	8,956	29,536
2	2.25	1.62	114,198	47,558	28,148	8,956	29,536
1	2.50	1.75	132,731	46,903	40,008	12,230	33,590
2	2.50	1.75	132,728	46,893	40,008	12,237	33,590

Table 5.6: Objective function breakdown for different electrification/PV scenarios and battery installation limits.

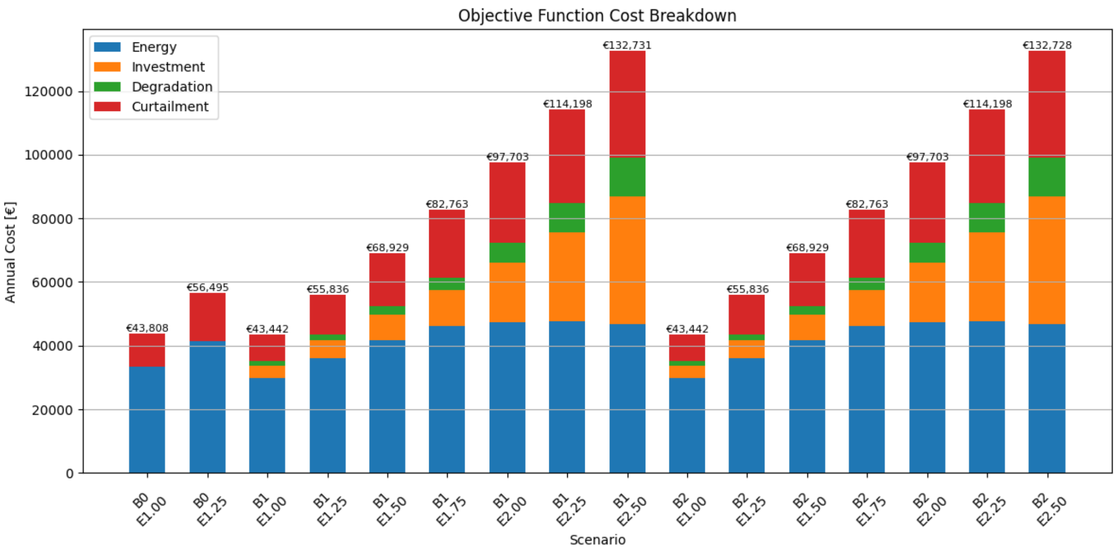

Figure 5.2: Objective cost breakdown into its four parts, for Scenario 3.

electrification levels are accompanied by higher PV penetration levels, resulting in larger amounts of photovoltaic generation becoming available throughout the network. This creates additional opportunities for energy shifting, allowing batteries to store energy that would otherwise be curtailed and discharge it during periods of higher demand. Consequently, the optimization model increasingly exploits storage not only to maintain network feasibility but also to improve the utilization of locally generated renewable energy.

This effect is reflected in the evolution of the objective components. Energy procurement costs increase only moderately despite the large growth in electricity demand. The results therefore suggest that a significant share of the additional PV generation is successfully absorbed by the battery systems and later utilized within the network.

Furthermore, the investment cost trajectory indicates that larger battery capacity becomes increasingly attractive at higher electrification levels. The investment costs at S3.E225 and S3E250 suggest that once a sufficiently large storage asset has been installed to address the primary network bottlenecks, additional PV energy can be integrated more efficiently using the existing storage infrastructure. As a result, a growing proportion of the available PV generation can be utilized rather than curtailed.

Finally, the results again demonstrate that allowing two batteries provides only limited additional value compared to allowing a single battery. Across nearly all scenarios, the total system costs and their individual components remain virtually identical for the one-battery and two-battery cases. This confirms the observations from the battery placement analysis: the optimization model is generally able to achieve the desired network performance using a single strategically located battery, while additional battery locations provide only marginal benefits under the considered network conditions.

5.2.3 Voltage Support Analysis with Batteries

To evaluate the impact of battery installation on network voltage performance, voltage statistics were calculated for every scenario.

Although the LinDistFlow model uses squared voltage magnitude $v_{i,t} = V_{i,t}^2$, all voltage results reported in Chapter 5 are converted back to voltage magnitude $V_{i,t} = \sqrt{v_{i,t}}$ and are therefore expressed in p.u. The reported voltage values are compared against the standard magnitude limits of 0.95 and 1.05 p.u.

The analysis is based on all hourly voltage measurements at all buses over the complete simulation horizon. To make the effect of increasing demand easier to observe, the results in Table 5.7 are grouped by electrification factor. The table summarizes the voltage behavior for all S3.E[100-250].B[0-2] scenarios.

For each scenario, the minimum, mean, and maximum voltage are reported. In addition, the 1st percentile (P1) and 99th percentile (P99) are included. These percentile values provide a more representative indication of the typical voltage range by reducing the influence of a small number of extreme observations. To identify the most critical location in the network, the 1st percentile voltage at each bus was calculated over the entire year. The bus with the lowest average 1st percentile voltage is reported as the weakest bus together with its average voltage magnitude.

Elec.	BESS	Min V	P1 V	Mean V	P99 V	Max V	Weakest Bus	P1 V (p.u.)
1.00	0	0.9814	1.0027	1.0201	1.0250	1.0267	39	0.9916
	1	0.9814	1.0029	1.0202	1.0262	1.0288	39	0.9918
	2	0.9814	1.0038	1.0202	1.0250	1.0260	39	0.9931
1.25	0	0.9703	0.9970	1.0189	1.0250	1.0275	39	0.9830
	1	0.9703	0.9974	1.0191	1.0267	1.0296	39	0.9833
	2	0.9703	0.9974	1.0191	1.0263	1.0293	39	0.9833
1.50	1	0.9646	0.9944	1.0180	1.0260	1.0291	39	0.9770
	2	0.9651	0.9944	1.0179	1.0250	1.0283	39	0.9772
1.75	1	0.9627	0.9895	1.0169	1.0278	1.0341	39	0.9690
	2	0.9627	0.9895	1.0169	1.0250	1.0301	39	0.9690
2.00	1	0.9613	0.9833	1.0160	1.0295	1.0391	42	0.9651
	2	0.9613	0.9833	1.0160	1.0257	1.0337	42	0.9651
2.25	1	0.9601	0.9783	1.0152	1.0304	1.0463	42	0.9640
	2	0.9529	0.9809	1.0151	1.0257	1.0300	39	0.9586
2.50	1	0.9563	0.9767	1.0144	1.0307	1.0451	39	0.9621
	2	0.9536	0.9761	1.0144	1.0267	1.0354	42	0.9578

Table 5.7: Voltage profile statistics grouped by electrification level and battery installation limit.

Several important trends can be observed from Table 5.7. Most notably, the optimization model becomes infeasible for all scenarios without battery storage from an electrification factor of 1.50 onwards. This indicates that, under the imposed voltage and line constraints, the network is no longer capable of accommodating the increasing demand and PV generation without additional flexibility. Consequently, battery storage is not merely beneficial under highly electrified conditions, but becomes a necessity for obtaining technically feasible network operation.

For the feasible scenarios, increasing electrification has a clear impact on network voltages. The minimum voltage decreases from 0.9814 p.u. in the baseline scenario to approximately 0.9536 p.u. in the most demanding scenarios, while the mean network voltage gradually declines from 1.0201 p.u. to around 1.0144 p.u. This demonstrates that increasing electrification systematically lowers the networks voltage, but stays within its operational voltage limits.

The percentile statistics show that low-voltage conditions become increasingly severe at higher electrification levels. The 1st percentile voltage decreases from 1.0027 p.u. in the baseline scenario to approximately 0.9761 p.u. at the highest electrification level. At the same time, the minimum voltage drops considerably faster than the percentile values, indicating that the most severe voltage problems occur during a relatively small number of hours. This suggests that undervoltage scenarios are driven by specific periods of high loading rather than by a general deterioration of the voltage profile throughout the year. However, the observed reduction in network voltages under heightened electrification is not the driver of network infeasibility, with the results suggesting that thermal loading plays an important role.

The location of the weakest bus also changes as network conditions become more demanding. For lower electrification levels, Bus 39 consistently exhibits the lowest voltage values. However, from an electrification factor of 2.0 onward, Bus 42 frequently becomes the weakest location in the network, where both Bus 39 and 42 are end-of-leaf nodes. This indicates that increasing loading changes the distribution of voltage stress throughout the feeder but keeps the most critical voltage conditions downstream.

The influence of battery installation is more subtle than that of increasing electrification. While batteries have only a limited effect on the minimum and average network voltage, they consistently reduce the highest voltages that occur during periods of high PV generation. For example, at an electrification factor of 2.25, the maximum voltage decreases from 1.0463 p.u. with one battery to 1.0300 p.u. with two batteries, with similar reductions observed for the 2.00 and 2.50 electrification scenarios. This trend is also reflected in the 99th percentile voltage, which consistently decreases when a second battery is installed. The results indicate that distributing storage across multiple locations is more effective than concentrating the same storage capacity at a single bus. By absorbing surplus PV generation closer to where it is produced, multiple batteries reduce localized power flows and thereby mitigate overvoltage conditions during peak hours.

5.2.3.1 Temporal Effect of the Battery on Voltage

To further investigate when battery storage contributes to voltage support, Figure 5.3 presents the average voltage profile and battery operation during the thirty most critical voltage days at Bus 38 for the E250PV175 scenario. This scenario is particularly relevant because Bus 38 was identified as one of the most voltage-sensitive locations in the network and is selected by the optimization model as the battery installation location.

A clear relationship can be observed between battery operation and the local voltage profile. During the early morning hours, the battery predominantly charges, coinciding with relatively low electricity demand and lower electricity prices. By absorbing energy from the network, the battery slightly increases local loading, which contributes to the observed voltage reductions. Around midday, when PV generation reaches its maximum, battery charging continues and helps absorb locally generated energy that would otherwise contribute to voltage rise within the network.

The battery subsequently discharges during the morning and evening demand peaks. In particular, the largest discharge events occur during the evening hours, when electricity demand is highest and the voltage at Bus 38 lowers. By injecting energy locally, the battery reduces the power that must be transported through the upstream feeder and therefore mitigates voltage drops at the end of the network.

Despite this contribution, the battery does not eliminate the evening voltage dip during the most critical days of the year under the heightened electrification scenario. Voltage magnitudes remain close to the lower operating limit, but stay within the allowable range throughout the illustrated period. Rather than preventing voltage violations, the battery provides local voltage support by discharging during periods of high demand, thereby increasing the voltage margin at the most vulnerable location in the feeder. Although the corresponding scenario without battery storage does not yield a feasible optimization solution, this infeasibility should not be attributed solely to undervoltage. Instead, it results from the combined network constraints, with evidence indicating that thermal loading of the feeder is the dominant bottleneck. The battery therefore contributes to restoring network feasibility by shaving the few critical peak-loading hours while simultaneously improving voltage conditions at the end of the feeder.

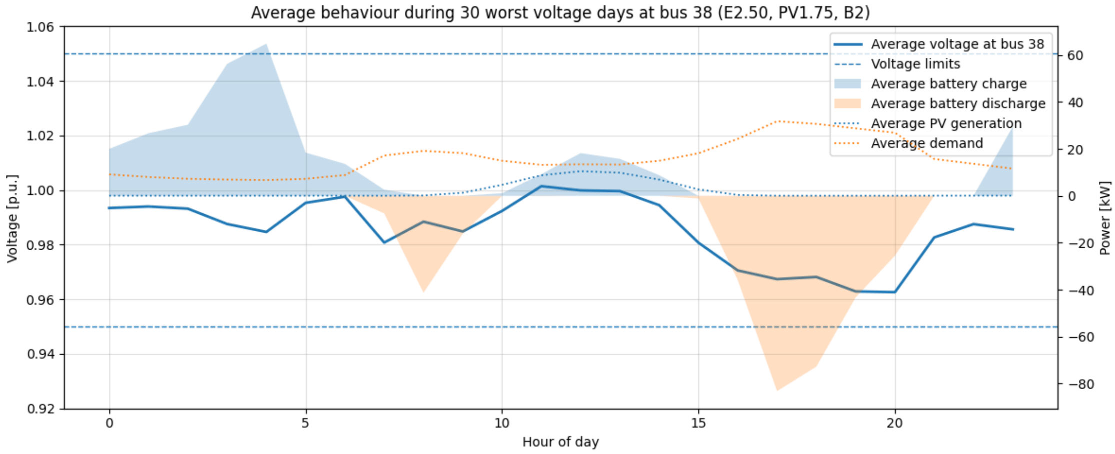

Figure 5.3: Average voltage profile and battery operation at Bus 38 during the thirty most critical voltage days for S3E250PV175.B2.

5.2.4 Line Loading Analysis

The previous sections showed that increasing electrification has a much larger impact on network performance than the number of installed batteries. To further investigate how the batteries influence power flows throughout the network, three line-loading comparisons are presented. Together, these figures illustrate the system-wide effect of increasing electrification, the local effect of battery placement, and the limited impact of batteries on the most heavily loaded line in the network.

The first comparison focuses on the root line connecting the slack bus (bus 129) to the root node (bus 14). Because all power imported from the upstream grid must pass through this line, it provides a useful indicator of overall network loading.

Figure 5.4 compares the base case S3.E100.B0 with the most heavily electrified feasible scenario S3.E250.B2. Under higher electrification, the loading distribution shifts toward higher values. The network requires substantially more energy from the substation, causing the loading distribution to move towards the right. The figure therefore confirms that increasing electrification has a direct impact on the utilization of the upstream connection and results in a more heavily loaded network overall. However, the line from 129 → 14, which also represents the transformer loading through the modeling decisions, shows that the transformer is never overloaded, not even in the highest electrified scenario.

To determine whether the root connection is representative of the broader network, Table 5.8 compares the 99th percentile loading of the ten most heavily loaded lines for scenarios with zero, one, and two installed batteries. The table confirms that battery installation has a limited influence on the loading of the most critical network branches. The five highest-ranked lines remain virtually unchanged, with only the root connection (129→14) showing a modest reduction in 99th percentile loading. In contrast, several downstream lines experience a slight increase in loading, reflecting the additional charging and discharging flows introduced by the batteries. These results suggest that battery storage primarily redistributes power flows locally, while leaving the dominant feeder loading largely unaffected.

Rank	From	To	B0 [%]	B1 [%]	B2 [%]
1	14	34	75.22	75.22	75.22
2	34	35	62.75	62.75	62.75
3	35	36	51.67	51.67	51.67
4	129	14	48.62	46.41	46.41
5	36	37	43.07	43.07	43.07
6	14	20	22.92	24.88	24.88
7	37	40	22.08	22.08	22.08
8	20	7	21.86	24.62	24.62
9	37	38	21.44	21.44	21.44
10	7	31	21.25	24.44	24.44

Table 5.8: Comparison of the 99th percentile line loading for the ten most critical lines under E125.

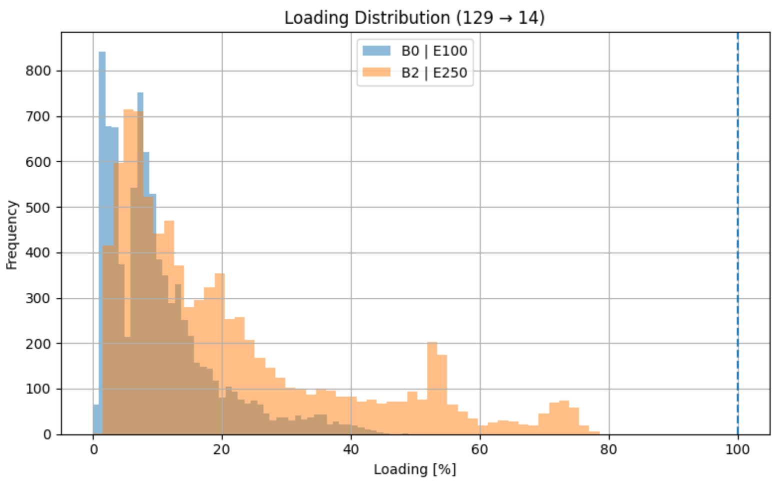

Figure 5.4: Loading distribution of the root line (bus 129 → 14) for the base scenario S3.E100.B0 and the highly electrified scenario S3.E250.B2.

The second comparison investigates the local effect of battery placement. Figure 5.5 shows the loading distribution of line 38 → 39 for scenarios S3.E150.B1 and S3.E150.B2. In the B1 case, the battery is installed at bus 41, while in the B2 case the battery is placed at bus 39.

The figure shows that the loading of line 38 → 39 increases considerably when a battery is installed at bus 39. This result is expected, as the battery must charge and discharge through the connecting line. Consequently, the line is utilized more frequently and at higher loading levels. Although the battery increases the local loading of this line, no line-loading violations are observed. The battery therefore changes the local power-flow pattern without creating additional congestion.

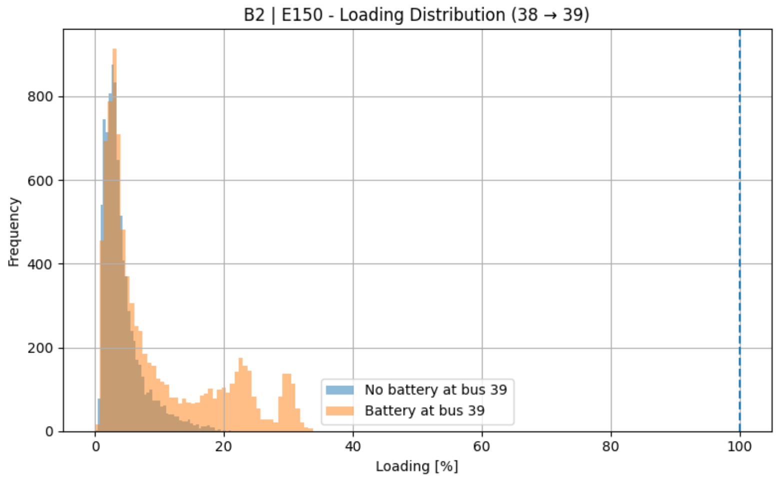

Figure 5.5: Loading distribution of line 38 → 39 for S3.E150.B1 and S3.E150.B2, illustrating the local impact of battery placement at bus 39.

Finally, Figure 5.6 examines the most heavily loaded line in the network, namely line 14 → 34. This line forms part of the main feeder connecting to buses with the heaviest demand of the network to the substation. The comparison is performed between S3.E250.B1 and S3.E250.B2.

Notably, line 14 → 34 is the most heavily loaded line in the network and is the most likely cause of network infeasibility in scenarios without battery storage. Unlike the previous example, the installation of an additional battery does not significantly reduce the loading of this line. Both distributions remain very similar and continue to approach the line loading limit. This suggests that a second battery provides no additional relief for this particular line. The reason is that line 14 → 34 acts as a primary connection between the substation and downstream demand. Regardless of where batteries are installed further downstream, a substantial amount of power must still pass through this line. As a result, the first battery appears to remove the few critical peak-loading hours that determine feasibility, while an additional battery has little further impact on the overall loading distribution of the most heavily loaded section of the feeder.

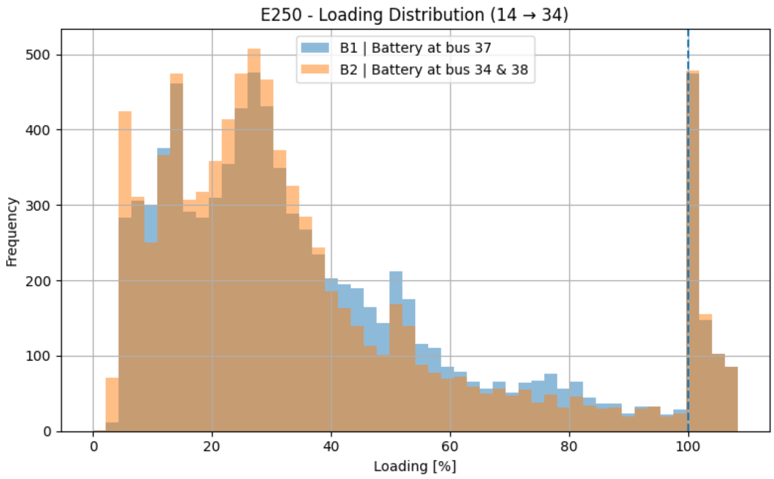

Figure 5.6: Loading distribution of the most heavily loaded line (bus 14 → 34) for S3.E250.B1 and S3.E250.B2.

Overall, the line-loading results indicate that increasing electrification has a strong impact on system-wide loading and identify the most heavily loaded line as the critical bottleneck within the network. Although batteries can substantially change the utilization of individual feeder sections, their impact on the loading distribution of this line remains limited. Instead, the results suggest that batteries primarily restore feasibility by reducing the few critical peak-loading hours, while this line continues to determine the network's loading limits.

5.3 PV Deployment Sensitivity Analysis

The previous section evaluated Battery Energy Storage System (BESS) placement and sizing under increasing electrification and photovoltaic (PV) penetration, assuming that PV generation was distributed proportionally across the network. This section investigates how different spatial distributions of PV generation influence optimal BESS placement and sizing, as well as PV utilization and curtailment. It additionally assesses the robustness of the battery placement decisions identified in Section 5.2.

Three PV allocation strategies are considered: (i) proportional allocation based on local electricity demand, (ii) concentration of PV at voltage-sensitive buses, and (iii) concentration of PV based on the Network Line Stability Index (NLSI). For each strategy, the annual PV energy budget is increased from 100% to 200% of total network demand in increments of 25%, while the electrification factor remains fixed at 1.0.

5.3.1 Battery Placement under PV Sensitivity Analysis

To investigate the sensitivity of battery placement decisions to different PV deployment assumptions, Table 5.9 presents the optimal BESS locations identified by the optimization model for each PV penetration level and PV allocation strategy, for both the single-battery and two-battery configurations. By comparing the selected buses across the Proportional, Voltage Severity, and NLSI-based allocation strategies, it becomes possible to determine whether alternative PV deployment assumptions lead to fundamentally different battery siting decisions.

Several clear patterns emerge from the results. First, for the single-battery configuration, Bus 25 becomes the dominant installation location at higher PV penetration levels, appearing in the majority of scenarios from PV150 onwards. Interestingly, Bus 25 is located at the end of a radial feeder branch, indicating that the optimization model frequently prefers storage installations at electrically remote locations where voltage deviations and congestion effects are most pronounced. Similar observations can be made for the alternative single-battery locations, such as Buses 24, 26, 27, and 29, which are also situated near the ends of feeder branches.

For the two-battery configuration, Buses 3 and 39 appear remarkably often across the tested scenarios. These buses are selected in the majority of the Proportional, Voltage Severity, and NLSI-based allocation cases, suggesting that they represent structurally advantageous battery locations rather than placements driven by a particular PV deployment strategy.

Scenario ID	PV Allocation	PV Factor	B=1 Location	B=2 Location(s)
S4.Prop.PV100	Proportional	1.00	24	3, 39
S4.Prop.PV125	Proportional	1.25	29	22, 24
S4.Prop.PV150	Proportional	1.50	25	3, 39
S4.Prop.PV175	Proportional	1.75	25	3, 39
S4.Prop.PV200	Proportional	2.00	25	3, 39
S4.Bus.PV100	Voltage Severity	1.00	26	3, 39
S4.Bus.PV125	Voltage Severity	1.25	27	0, 5
S4.Bus.PV150	Voltage Severity	1.50	25	12, *no* 2^{nd}*battery*
S4.Bus.PV175	Voltage Severity	1.75	25	3, 39
S4.Bus.PV200	Voltage Severity	2.00	26	3, 39
S4.Line.PV100	Line Stability	1.00	25	3, 39
S4.Line.PV125	Line Stability	1.25	24	3, 39
S4.Line.PV150	Line Stability	1.50	24	3, 39
S4.Line.PV175	Line Stability	1.75	25	1, 4
S4.Line.PV200	Line Stability	2.00	25	3, 39

Table 5.9: Optimal BESS locations under different PV allocation strategies and PV penetration levels.

Only a limited number of scenarios deviate from this general pattern. Specifically, the scenarios S4.Bus.PV125, S4.Bus.PV150, and S4.Line.PV175 produce alternative battery placements. However, even in these cases, the selected buses remain located at the extremities of the radial network.

Overall, the results indicate that battery placement decisions are relatively robust to the alternative PV allocation assumptions considered here. While individual battery locations occasionally change, the optimization repeatedly selects a small set of structurally important end-of-feeder buses. Consequently, the findings indicate that uncertainty regarding the spatial distribution of future PV installations has a limited impact on the resulting BESS siting decisions within the studied network.

5.3.2 Battery Sizing Under PV Sensitivity Analysis

To evaluate the sensitivity of BESS sizing decisions to alternative PV deployment assumptions, this subsection reports the total installed battery energy and power capacity for each PV penetration level and PV allocation strategy. Since the single-battery scenarios resulted in identical capacities across all allocation methods, only the two-battery cases are presented.

Table 5.10 shows that the total installed battery capacity increases steadily with increasing PV penetration levels. Across all three PV allocation strategies, the required storage capacity grows from approximately 102 kWh at PV100 to approximately 231 kWh at PV200. A similar trend is observed for the installed power rating, which increases from roughly 25 kW to 58 kW.

Scenario ID	PV Allocation	Total Energy [kWh]	Total Power [kW]
PV100			
S4.Prop.PV100	Proportional	101.83	25.46
S4.Bus.PV100	Voltage Severity (Bus)	101.83	25.46
S4.Line.PV100	Line Stability (NLSI)	101.83	25.46
PV125			
S4.Prop.PV125	Proportional	137.62	34.40
S4.Bus.PV125	Voltage Severity (Bus)	137.62	34.41
S4.Line.PV125	Line Stability (NLSI)	137.62	34.41
PV150			
S4.Prop.PV150	Proportional	177.18	44.29
S4.Bus.PV150	Voltage Severity (Bus)	177.18	44.29
S4.Line.PV150	Line Stability (NLSI)	177.17	44.30
PV175			
S4.Prop.PV175	Proportional	203.86	50.97
S4.Bus.PV175	Voltage Severity (Bus)	203.86	50.97
S4.Line.PV175	Line Stability (NLSI)	203.86	50.97
PV200			
S4.Prop.PV200	Proportional	230.99	57.74
S4.Bus.PV200	Voltage Severity (Bus)	230.99	57.75
S4.Line.PV200	Line Stability (NLSI)	230.99	57.75

Table 5.10: Optimal BESS sizing for scenarios with a battery budget of two units.

More importantly, the differences between the three PV allocation strategies are negligible. For every PV penetration level, the resulting energy capacities are either identical or differ only by rounding effects. The same observation holds for the corresponding power ratings. This indicates that the optimization model consistently selects nearly the same total amount of storage regardless of whether PV generation is distributed proportionally, concentrated at voltage-sensitive buses, or allocated according to the NLSI-based line stability ranking.

These results suggest that optimal BESS sizing is primarily driven by the total amount of PV generation connected to the network rather than by its exact spatial distribution. While the PV allocation strategy may influence local congestion patterns and battery placement decisions, it has little effect on the overall storage capacity required to accommodate increasing PV penetration levels. Consequently, the sizing component of the BESS investment decision appears robust to the alternative PV deployment assumptions considered in this sensitivity analysis.

5.3.3 PV Curtailment under PV Sensitivity Analysis

The previous sections demonstrated that the optimal battery locations remain relatively stable across alternative PV deployment strategies and that the total installed battery capacity is primarily driven by the overall PV penetration level. To further understand the operational impact of these deployment assumptions, this section investigates how photovoltaic generation is utilized within the network.

Specifically, the analysis focuses on the proportion of generated PV energy that can be directly utilized and the proportion that must be curtailed due to network limitations. Comparing these metrics across the Proportional, Voltage Severity, and NLSI-based allocation strategies provides additional insight into whether alternative PV deployment assumptions affect the network's ability to accommodate increasing levels of distributed PV generation.

Several observations can be made from Table 5.3.3. First, increasing PV penetration leads to a consistent reduction in the fraction of PV energy that can be utilized within the network. For the Proportional allocation strategy without batteries (B0), the utilized share decreases from 19.30% at PV100 to only 12.25% at PV200, while curtailment increases from 80.70% to 87.75%. Similar trends are observed for the Voltage Severity and NLSI-based allocation strategies.

Second, the installation of battery storage substantially increases PV utilization across all penetration levels. For example, under the Proportional allocation strategy, the utilized PV share increases from 19.30% to 25.02% at PV100 and from 12.25% to 19.46% at PV200 when two batteries are installed. This corresponds to utilization improvements of approximately 30% and 59%, respectively, relative to the no-battery case.

Most importantly, the differences between the three PV allocation strategies are negligible. For every PV penetration level, the utilized and curtailed shares differ by less than 0.1 percentage points between the Proportional, Voltage Severity, and NLSI-based scenarios. This indicates that the aggregate amount of PV energy utilized by the network is largely insensitive to the specific spatial distribution of PV generation.

These results suggest that overall PV penetration is the dominant factor determining PV utilization and curtailment levels, whereas the tested PV allocation strategies have only a limited influence on aggregate network performance. Because electricity export is disabled in this study, aggregate PV surplus rather than the spatial allocation of PV

Scenario ID	PV Strategy	BESS	PV Used (%)	PV Curtailed (%)
PV100				
S4.Prop.PV100.B0	Proportional	0	19.30	80.70
S4.Prop.PV100.B2	Proportional	2	25.02	74.98
S4.Bus.PV100.B0	Voltage Severity	0	19.35	80.65
S4.Bus.PV100.B2	Voltage Severity	2	25.02	74.98
S4.Line.PV100.B0	NLSI	0	19.33	80.67
S4.Line.PV100.B2	NLSI	2	25.01	74.99
PV125				
S4.Prop.PV125.B0	Proportional	0	16.76	83.24
S4.Prop.PV125.B2	Proportional	2	23.17	76.83
S4.Bus.PV125.B0	Voltage Severity	0	16.82	83.18
S4.Bus.PV125.B2	Voltage Severity	2	23.16	76.84
S4.Line.PV125.B0	NLSI	0	16.79	83.21
S4.Line.PV125.B2	NLSI	2	23.14	76.86
PV150				
S4.Prop.PV150.B0	Proportional	0	14.89	85.11
S4.Prop.PV150.B2	Proportional	2	21.94	78.06
S4.Bus.PV150.B0	Voltage Severity	0	14.95	85.05
S4.Bus.PV150.B2	Voltage Severity	2	21.93	78.07
S4.Line.PV150.B0	NLSI	0	14.93	85.07
S4.Line.PV150.B2	NLSI	2	21.92	78.08
PV175				
S4.Prop.PV175.B0	Proportional	0	13.44	86.56
S4.Prop.PV175.B2	Proportional	2	20.55	79.45
S4.Bus.PV175.B0	Voltage Severity	0	13.48	86.52
S4.Bus.PV175.B2	Voltage Severity	2	20.55	79.45
S4.Line.PV175.B0	NLSI	0	13.46	86.54
S4.Line.PV175.B2	NLSI	2	20.54	79.46
PV200				
S4.Prop.PV200.B0	Proportional	0	12.25	87.75
S4.Prop.PV200.B2	Proportional	2	19.46	80.54
S4.Bus.PV200.B0	Voltage Severity	0	12.30	87.70
S4.Bus.PV200.B2	Voltage Severity	2	19.46	80.54
S4.Line.PV200.B0	NLSI	0	12.28	87.72
S4.Line.PV200.B2	NLSI	2	19.46	80.54

Table 5.11: PV utilization and curtailment under alternative PV deployment strategies.

largely determines the amount of curtailment. Under an export-enabled operating regime, the spatial allocation of PV may have a stronger influence on local network constraints and the resulting curtailment.

Figure 5.7 illustrates the utilization and curtailment of photovoltaic generation under the Proportional PV allocation strategy. For each PV penetration level, the figure compares the cases without battery storage (B0) and with two batteries installed (B2). The blue portion of each bar represents the amount of PV energy utilized within the network, while the orange portion represents curtailed PV energy. The total annual PV generation is indicated above each bar, and the utilized PV energy is shown within the blue section.

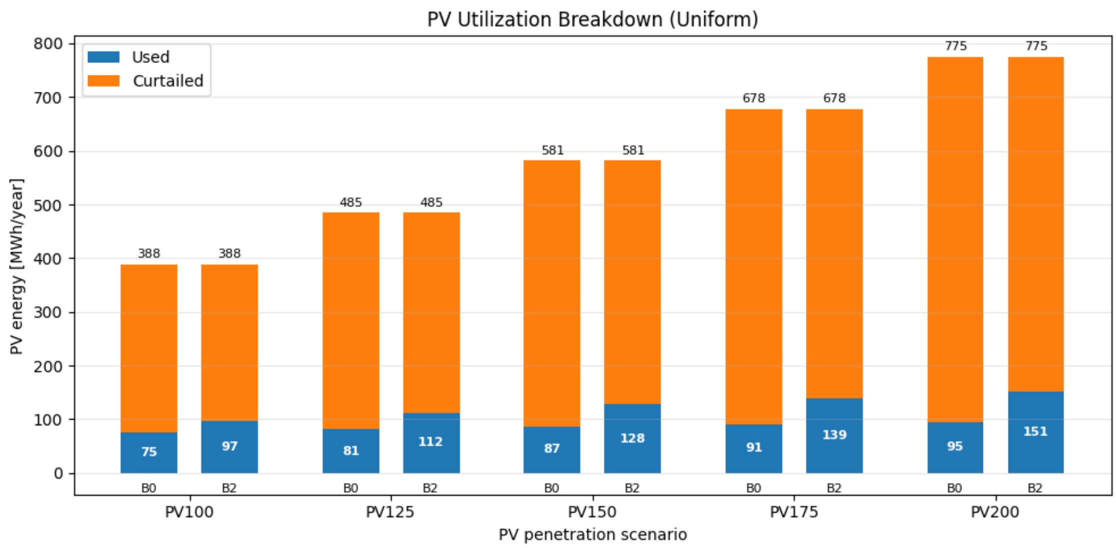

Figure 5.7: PV utilization and curtailment under the Proportional PV allocation strategy.

The figure provides additional insight into how increasing PV penetration affects the balance between utilized and curtailed PV energy. As the PV penetration factor increases from PV100 to PV200, total annual PV generation approximately doubles, increasing from 388 MWh to 775 MWh. However, the amount of utilized PV energy increases only modestly, from approximately 75 MWh to 95 MWh in the absence of battery storage and from approximately 97 MWh to 151 MWh when two batteries are installed.

Consequently, most of the additional PV generation introduced at higher penetration levels is curtailed rather than utilized. This indicates that the network reaches its hosting capacity limits relatively quickly, after which additional PV installations contribute increasingly to curtailment. While battery storage consistently increases the amount of utilized PV energy, the improvement is insufficient to fully absorb the growing PV surplus at higher penetration levels.

The figure therefore highlights two important findings. First, battery storage effectively increases PV utilization across all scenarios. Second, the benefits of battery storage become increasingly constrained as PV penetration continues to grow, suggesting that larger storage capacities or additional network reinforcement measures would be required to accommodate substantially higher levels of PV generation without significant curtailment.

5.3.4 The Timing of PV Curtailment

This section investigates when PV curtailment occurs and what drives it. Figures 5.8 and 5.9 present the monthly curtailed PV energy for the Proportional PV allocation strategy under different PV penetration levels. In addition, the figures show the average monthly electricity price and the average price during the lowest 10% of hourly price observations for that month, providing context regarding the economic conditions under which curtailment occurs.

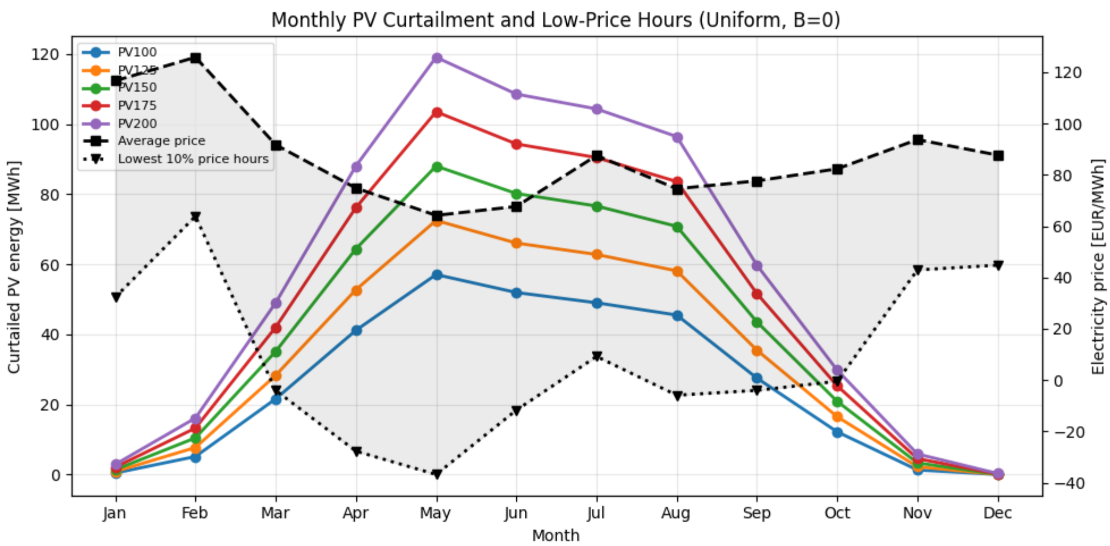

Figure 5.8: Monthly curtailed PV energy for different PV penetration levels under the Proportional PV allocation strategy without battery storage ($B = 0$).

Figure 5.8 shows that curtailment follows a strong seasonal pattern. For all PV penetration levels, curtailed energy remains limited during winter months, increases rapidly during spring, reaches its highest values between May and August, and subsequently declines towards the end of the year. This behavior reflects the seasonal availability of solar generation, with surplus production occurring primarily during periods of high irradiance.

The magnitude of curtailment increases almost proportionally with PV penetration. While the PV100 scenario experiences relatively modest curtailment, the PV175 and PV200 scenarios exhibit substantial energy losses during the summer period. For the PV200 case, monthly curtailed energy approaches 120 MWh during the peak months, indicating that a significant fraction of additional PV generation cannot be accommodated by local demand alone.

A comparison with the electricity price indicators reveals that the largest curtailment volumes occur during months in which the lowest-priced hours are close to or below zero. The high curtailment volumes are primarily caused by periods of surplus PV generation that exceed the local demand and storage capacity. At the same time, these periods often coincide with wider system-wide renewable abundance, resulting in lower electricity prices. Consequently, the economic penalty associated with curtailment is relatively low in May.

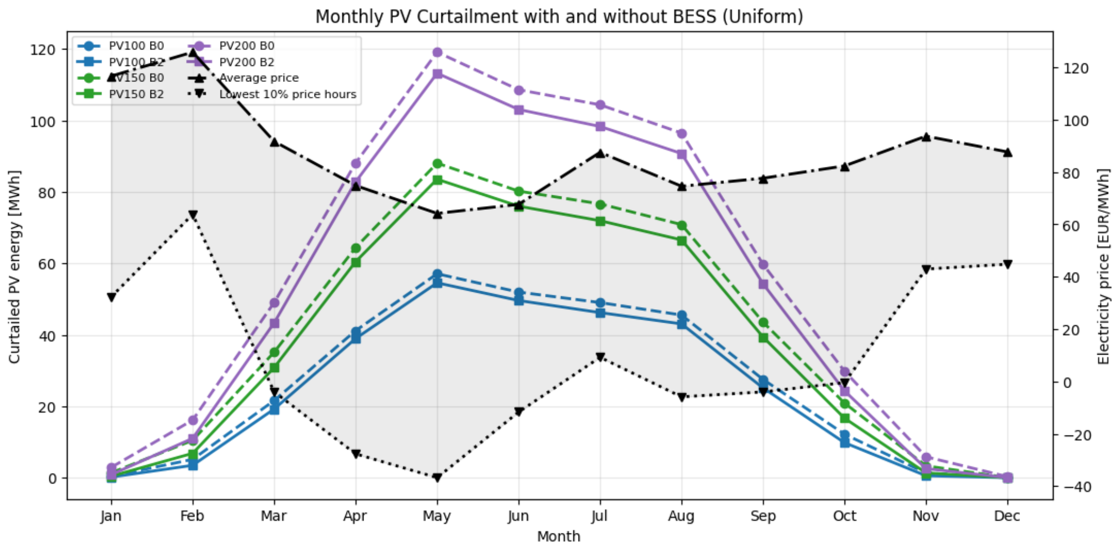

Figure 5.9: Monthly curtailed PV energy for different PV penetration levels under the Proportional PV allocation strategy with two batteries installed ($B = 2$).

Figure 5.9 compares monthly PV curtailment with and without battery storage for PV penetration levels of 100%, 150%, and 200%. Across all PV levels, the dashed lines represent the case without batteries, while the solid lines represent the case with two batteries. The results show that battery storage consistently reduces PV curtailment, but does not fundamentally change the seasonal pattern. Curtailment remains concentrated in spring and summer, when PV generation is highest.

The reduction is most visible during the months with the highest curtailed energy, particularly between April and August. For example, the PV200 scenario still reaches its maximum curtailment in May, but the peak is lower when two batteries are installed. This indicates that storage increases local PV utilization by absorbing part of the surplus generation. However, the remaining curtailment levels show that the batteries are not sufficient to fully accommodate the PV deployment levels considered in this study.

Overall, the results demonstrate that increasing PV penetration substantially increases curtailment volumes, particularly during periods of high solar availability. Battery storage mitigates part of this effect by shifting excess generation across time, thereby improving PV utilization. However, under the no-export assumption adopted in this study, curtailment remains unavoidable at high PV penetration levels, suggesting that additional flexibility measures or export capabilities would be required to fully utilize the available renewable generation.

5.3.5 PV Usage

To illustrate how battery storage improves photovoltaic (PV) utilization, Figures 5.10 and 5.11 compare the average daily demand profile, PV generation profile, and utilized PV energy under the Voltage Severity allocation strategy for the PV100 and PV200 scenarios. The figures contrast the cases without battery storage ($B = 0$) and with two installed batteries ($B = 2$), highlighting how increasing PV penetration affects the utilization of locally generated solar energy.

Figures 5.10 and 5.11 clearly illustrate the structural mismatch between electricity demand and PV generation. Demand reaches its highest levels during the evening, whereas PV generation peaks around midday when electricity consumption is relatively low. Increasing the PV penetration from PV100 to PV200 approximately doubles the midday generation peak while demand remains virtually unchanged, substantially increasing the surplus of locally generated electricity. Consequently, battery storage becomes increasingly valuable by shifting part of this excess generation towards the late afternoon and evening hours, resulting in visibly higher PV utilization in the $B = 2$ scenarios.

Table 5.12 quantifies the hourly increase in utilized PV energy resulting from the installation of two batteries under the Voltage Severity allocation strategy.

The battery impact (as shown in Table 5.12) is concentrated entirely during daylight hours, when photovoltaic generation is available. Under the PV100 scenario, PV utilization

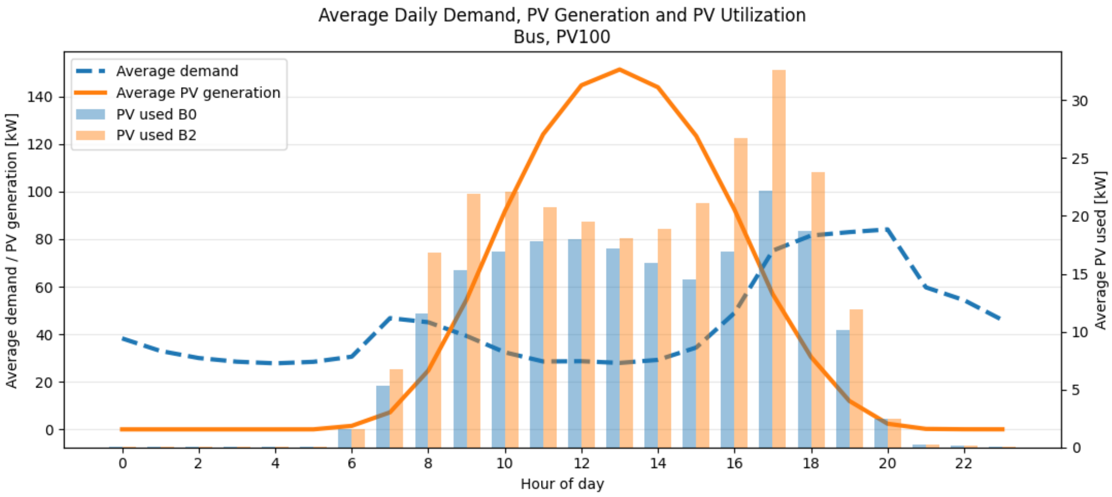

Figure 5.10: Average daily demand profile, PV generation profile, and utilized PV energy under the Voltage Severity (Bus) allocation strategy for the PV100 scenario.

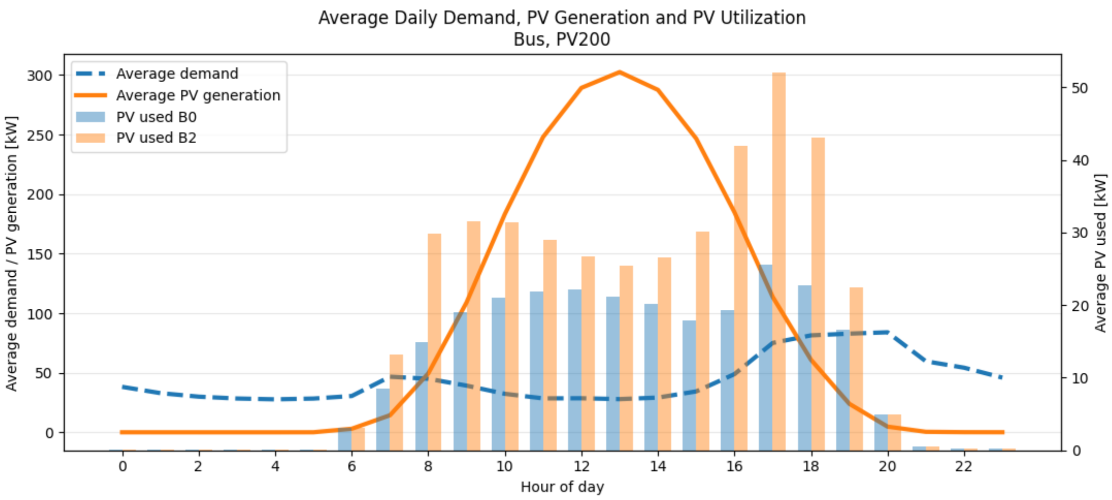

Figure 5.11: Average daily demand profile, PV generation profile, and utilized PV energy under the Voltage Severity (Bus) allocation strategy for the PV200 scenario.

Hour	S4.Bus.PV100			S4.Bus.PV200		
	B0 [kW]	B2 [kW]	Δ [%]	B0 [kW]	B2 [kW]	Δ [%]
07:00	5.32	6.80	27.69	8.50	13.20	55.17
08:00	11.60	16.79	44.81	14.91	29.82	100.03
09:00	15.34	21.87	42.57	19.04	31.56	65.77
10:00	16.91	22.06	30.45	21.02	31.48	49.80
11:00	17.83	20.74	16.31	21.95	29.00	32.11
12:00	18.01	19.49	8.20	22.17	26.68	20.37
13:00	17.16	18.09	5.47	21.23	25.46	19.92
14:00	15.95	18.87	18.30	20.22	26.62	31.68
15:00	14.48	21.08	45.63	17.91	30.19	68.56
16:00	16.94	26.71	57.63	19.39	41.97	116.46
17:00	22.18	32.58	46.88	25.65	52.01	102.73
18:00	18.71	23.79	27.15	22.78	43.12	89.32
19:00	10.18	11.92	17.13	16.64	22.44	34.86
Average			**29.40**			**60.52**

Table 5.12: Hourly PV utilization increase from two batteries under the Voltage Severity allocation strategy.

increases by an average of 29.4%, with the largest improvements occurring between 15:00 and 18:00. During this period, utilization increases by up to 57.6%, demonstrating that batteries effectively shift surplus midday generation towards periods of higher electricity demand.

The effect becomes considerably stronger under the PV200 scenario. Average PV utilization increases by 60.5%, more than double the improvement observed for PV100. During the late afternoon, utilization exceeds 100% improvements at both 16:00 (116.5%) and 17:00 (102.7%), indicating that more PV energy can be recovered when larger daytime surpluses are available. These results confirm that the value of battery storage increases as photovoltaic penetration grows and curtailment becomes more severe.

5.4 Economic Sensitivity Analysis Results

The economic sensitivity analysis investigates how the profitability of battery storage depends on electricity market conditions. Unlike the previous experiments, which evaluated the technical performance of battery storage under different network configurations, this analysis keeps the operational decisions fixed and recalculates the annual system costs using historical Dutch day-ahead electricity prices from 2016 up and until 2025. By evaluating the same battery dispatch and operation under different market conditions, the analysis isolates the influence of electricity price dynamics on the economic value of battery storage.

Year	Min	P1	Mean	P99	Max	P99–P1 Spread
2015	1.67	15.49	40.03	66.57	99.77	51.09
2016	2.79	12.86	32.25	67.99	135.00	55.13
2017	1.74	19.45	39.31	86.97	151.07	67.52
2018	0.55	22.03	52.53	93.43	175.00	71.40
2019	-9.02	18.26	41.20	77.13	121.46	58.87
2020	-79.19	-0.19	32.24	77.44	200.04	77.63
2021	-66.18	0.01	102.96	360.62	620.00	360.61
2022	-222.36	0.00	241.92	644.67	871.00	644.67
2023	-500.00	-12.97	95.82	208.13	463.77	221.10
2024	-200.00	-30.02	77.29	206.27	872.96	236.29
2025	-350.00	-20.00	86.81	217.06	523.47	237.06

Table 5.13: Summary statistics of Dutch day-ahead electricity prices for the period 2015–2025.

Table 5.13 and Figure 5.12 show that Dutch electricity markets experienced a clear structural shift during the considered period. Between 2015 and 2020, annual price volatility remained relatively limited, with a P99–P1 spread ranging between approximately 51 and 78 EUR/MWh. From 2021 onwards, price volatility increased dramatically, reaching 361 EUR/MWh in 2021 and peaking at 645 EUR/MWh in 2022. Although volatility declined after 2022, it remained substantially higher than during the pre-2021 period. These results demonstrate that recent electricity markets provide considerably larger differences between low-price and high-price periods.

Table 5.4 presents the annual system costs for the battery-free case (B0) and the two-battery case (B2). Results are reported both including and excluding the PV curtailment penalty. The values including the curtailment penalty correspond to the optimization objective defined in Chapter 3. Since electricity export is disabled throughout this study, the curtailment penalty represents a modeling approximation rather than a direct financial cost. The values excluding the curtailment penalty therefore provide the direct financial comparison, consisting only of electricity purchase costs together with annualized battery investment and degradation costs.

The annual system costs shown in Table 5.4 increase substantially during years with high electricity prices, particularly in 2021 and 2022. Table 5.4 shows that battery storage reduces the optimization objective only in 2022 and 2025 when the curtailment penalty is included. However, after excluding the curtailment penalty, battery storage remains

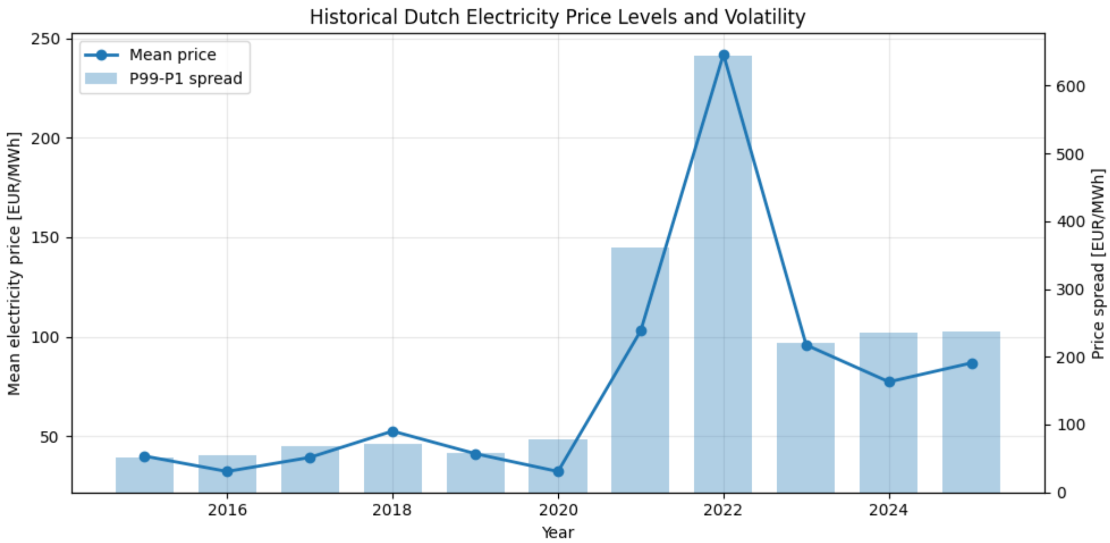

Figure 5.12: Evolution of average Dutch day-ahead electricity prices and annual price volatility between 2015 and 2025. Price volatility is represented by the difference between the 99th and 1st percentile electricity prices.

economically beneficial only in 2022. In all other years, the reduction in electricity purchase costs is insufficient to offset the additional investment and degradation costs of the battery. The avoided curtailment penalty becomes larger in years with higher electricity prices, increasing from approximately EUR 700–1,200 before 2021 to around EUR 2,000 in the more recent years.

These results demonstrate that the economic value of battery storage depends primarily on electricity price volatility rather than on the average electricity price level. During years with limited price fluctuations, the achievable savings through energy arbitrage are too small to recover the battery investment and degradation costs. Only the highly volatile market conditions observed in 2022 generate sufficient arbitrage opportunities for battery storage to become economically attractive without relying on the curtailment penalty. The small cost reduction observed for 2025 in the optimization objective is therefore explained by the reduction in the modeling penalty for PV curtailment, rather than by direct financial savings. Consequently, the technical battery sizing and operation remain unchanged throughout this analysis, while their economic value is highly dependent on the prevailing electricity market conditions.

Year	Including curtailment [€]		Excluding curtailment [€]	
	B0	B2	B0	B2
2015	25,226	28,464	12,777	16,987
2016	20,727	24,445	11,131	15,582
2017	24,853	28,246	13,693	17,963
2018	33,804	36,448	17,183	21,073
2019	25,526	28,763	13,842	18,036
2020	19,058	22,653	11,886	16,199
2021	60,891	61,518	40,060	42,687
2022	146,958	138,940	78,036	75,893
2023	55,307	55,359	34,518	36,712
2024	42,777	43,713	29,421	31,993
2025	43,808	43,442	33,454	35,048

Table 5.14: Annual system costs for the baseline scenario (S3.E100), comparing the battery-free case (B0) and the two-battery case (B2).

Year	Including curtailment (%)	Excluding curtailment (%)	Curtailment reduction [EUR]
2015	12.84	32.95	972
2016	17.94	39.98	732
2017	13.65	31.18	877
2018	7.82	22.64	1,245
2019	12.68	30.29	956
2020	18.86	36.29	718
2021	1.03	6.56	2,001
2022	-5.46	-2.75	5,874
2023	0.09	6.35	2,141
2024	2.19	8.74	1,636
2025	-0.84	4.76	1,960

Table 5.15: Relative economic impact of battery storage under historical electricity price conditions, results are reported both including and excluding the PV curtailment penalty.

6

Discussion

This chapter discusses the findings presented in Chapter 5 by interpreting them in relation to the existing literature and the broader challenges associated with congestion management in low-voltage distribution networks. Rather than revisiting the results on a per-experiment basis, the discussion synthesizes the main findings across the different research questions to identify the key insights that emerge from this study.

The evaluation demonstrated that the proposed optimization framework successfully determines battery placement, sizing, and operation while explicitly accounting for network constraints, photovoltaic generation, and electricity market conditions. Although each experiment focused on a different aspect of the problem, several consistent patterns emerged across the results. These recurring observations provide a broader understanding of how Battery Energy Storage Systems contribute to congestion mitigation and under which conditions they are most effective.

The discussion is therefore structured around five overarching themes: the influence of network topology, the relationship between battery placement and sizing, the effectiveness of storage for congestion mitigation, the potential of batteries to substitute grid reinforcement, and the economic implications under varying market conditions. For each of the themes, the theoretical and practical implications are outlined. The theoretical implications either align with the literature or advance the literature for the Dutch specific case, as well as the practical implications that advise service operators. The chapter concludes by discussing the limitations of the present study and identifying opportunities for future research.

6.1 Network topology dominates optimization

One of the most consistent findings throughout this study is that the electrical topology of the evaluated distribution network appears to be the dominant factor determining the optimal battery placement. Across the baseline congestion analysis, the battery placement optimization, and the PV deployment sensitivity analysis, the optimization repeatedly selected nearly identical battery locations despite substantial variations in photovoltaic penetration levels and PV allocation strategies. Likewise, the same buses consistently exhibited the largest voltage deviations and the same lines repeatedly emerged as the most heavily loaded components of the network.

This consistency suggests that, for the evaluated scenarios, the optimization is driven primarily by the structural characteristics of the radial network rather than by the specific operating scenario. The identified battery locations were almost exclusively situated at electrically weak leaf nodes located near the ends of feeders, where voltage drops accumulate and the electrical distance from the transformer is greatest. Installing storage at these locations therefore appears to provide the greatest benefit for mitigating local voltage deviations while simultaneously reducing power flows through downstream branches.

The robustness of the optimal battery locations under varying PV deployment scenarios further suggests that, for the evaluated network, topology has a considerably stronger influence on battery siting than the spatial distribution of distributed PV generation.. Although increasing PV penetration changes the magnitude of power injections throughout the network, it does not fundamentally alter the underlying electrical weaknesses of the feeder.Instead, higher PV penetration appears to primarily intensify congestion at locations that are already structurally vulnerable. Consequently, the optimization continues to identify the same electrically critical buses while adapting the battery capacities to accommodate the increased network stress.

These findings are consistent with previous studies that identify feeder-end locations as the most effective positions for battery installation in radial distribution systems (2, 3, 6, 7). Rather than creating entirely new congestion patterns, increasing distributed generation tends to amplify existing voltage-sensitive areas that are already constrained by network topology (1, 5). The results, therefore, reinforce the view that electrical characteristics such as feeder depth, impedance, and radial structure remain the primary determinants of optimal storage placement.

From a practical perspective, this robustness offers an important advantage for distribution system operators. Since the optimal battery locations remain largely unchanged across the evaluated PV deployment scenarios, the results suggest that long-term storage planning may focus on identifying structurally weak locations within the network instead of repeatedly optimizing battery siting for every anticipated future scenario. While storage capacities may need to evolve as electricity demand and distributed generation increase, the physical locations where storage provides the greatest network benefit appear to remain remarkably stable.

6.2 Battery sizing is adaptive, placement is robust

A second important finding of this study is the clear distinction between the robustness of battery placement and the adaptability of battery sizing. While the optimization consistently selected nearly identical installation locations across different scenarios, the corresponding battery capacities varied substantially as electrification levels and photovoltaic penetration changed. This suggests that the optimization problem is governed by two fundamentally different mechanisms: network topology determines where storage provides the greatest technical benefit, whereas the severity of network congestion determines how much storage capacity is required.

The results show that battery capacity increases as the network becomes more heavily stressed. Higher levels of photovoltaic generation create larger surplus energy during periods of high solar production, requiring additional storage capacity to absorb excess generation and reduce curtailment costs. Similarly, increasing electrification raises local demand and power flows, increasing the amount of energy that must be shifted to alleviate voltage deviations and line loading. Rather than relocating storage assets, the optimization responds by increasing the size of batteries installed at the already identified electrically critical locations.

This distinction has important implications for distribution network planning. Most optimization-based BESS planning studies determine battery location and capacity simultaneously, recognizing that both decisions are interdependent in achieving technical and economic objectives (2, 3). While this joint optimization remains essential, the results of this study indicate that the two decision variables are driven by different underlying factors. Battery siting appears to be largely determined by the electrical topology of the network and therefore remains relatively insensitive to changes in future demand and PV deployment. In contrast, the optimal battery capacity responds directly to the severity of network congestion, increasing as higher demand and PV penetration place greater stress on the distribution network. Consequently, battery placement and sizing should not only be optimized jointly, but also interpreted as complementary decisions that exhibit fundamentally different sensitivities to future operating conditions.

This observation also reinforces the importance of battery sizing as a decision variable within optimization models, aligning with the literature (2, 3, 9). The present results illustrate why this approach is necessary. Fixing battery capacities beforehand may underestimate the storage required under highly stressed operating conditions, while simultaneously leading to unnecessary investment when future network loading remains moderate. By allowing storage capacity to emerge as an optimization variable, the model continuously balances investment costs against operational benefits, producing battery sizes that adapt to the technical requirements of each scenario while maintaining economically efficient solutions.

From a practical perspective, this suggests that distribution system operators can identify strategically valuable battery locations relatively early in the planning process, while delaying final investment decisions regarding storage capacity until future demand growth and photovoltaic adoption become more certain.

6.3 Storage provides local congestion relief but does not replace grid reinforcement

The evaluation demonstrates that, within the evaluated network, BESS are highly effective at mitigating local congestion but considerably less effective at resolving system-wide network constraints. Throughout the evaluated scenarios, battery installation consistently improved voltage profiles at electrically weak buses and reduced loading on nearby distribution lines. These improvements were most pronounced at the feeder ends where batteries were installed, confirming that storage primarily influences the local electrical environment by shifting energy in time and reducing power flows through downstream network components.

In contrast, the impact of storage on the overall network remained more limited. The analysis of line loading showed that batteries produced only minor reductions in loading on the primary feeder connected to the transformer, while structurally critical network bottlenecks remained largely unchanged. Likewise, although batteries consistently reduced photovoltaic curtailment, particularly during periods of high solar generation, substantial curtailment persisted under high PV penetration levels. The seasonal mismatch between concentrated summer PV production and relatively low local electricity demand therefore remained evident, even after storage was introduced.

These findings indicate that battery storage primarily redistributes existing energy within the network rather than increasing the physical transfer capacity of the electricity infrastructure. By charging during periods of local generation surplus and discharging during periods of increased demand, batteries alleviate local voltage violations and reduce congestion on nearby feeder sections. However, they cannot fundamentally remove the structural limitations arising from cable capacities and the underlying radial topology of the evaluated distribution network.

This observation is consistent with previous research, which identifies battery storage as an effective flexibility resource for delaying or mitigating congestion, rather than as a complete substitute for conventional grid reinforcement (2, 3). The results, therefore, suggest that storage should primarily be regarded as a complementary congestion management measure. While strategically placed batteries can substantially improve network operation and increase the effective utilization of existing infrastructure, the results suggest that future low-voltage networks with continued electrification and high photovoltaic penetration may require a combination of storage deployment, active network management, and targeted grid reinforcement to accommodate long-term growth.

6.4 Economic feasibility depends on markets, not network physics

The economic sensitivity analysis showed that the technical optimization results remained unchanged across the evaluated electricity price scenarios, while the financial performance of battery storage varied considerably. The same battery locations and capacities continued to provide the greatest technical benefit for congestion mitigation, yet their economic viability ranged from clearly unprofitable during periods of stable electricity prices to profitable during years characterized by high price volatility.

These findings highlight that the technical value and economic value of battery storage should be considered separately. From a network perspective, batteries consistently improve voltage profiles, reduce local line loading, and increase the utilization of photovoltaic generation.However, whether these technical benefits justify the required investment depends strongly on the prevailing electricity market conditions and on whether avoided PV curtailment is assigned an economic value within the optimization objective. As demonstrated by the sensitivity analysis, volatile electricity markets create additional arbitrage opportunities that can substantially improve the business case for battery deployment.

Consequently, the results suggest that investment decisions regarding battery storage should not be based solely on current market conditions. While profitability may fluctuate as electricity markets evolve, the underlying technical need for flexibility within increasingly congested distribution networks remains. Battery storage should therefore be evaluated both as a congestion management asset and as an economic investment, recognizing that technical performance is primarily determined by network conditions, whereas economic performance depends on electricity market conditions and the valuation of avoided PV curtailment.

6.5 Limitations

Although this study provides valuable insights into the optimal placement, sizing, and operation of Battery Energy Storage Systems in low-voltage distribution networks, several limitations should be acknowledged:

First, the case study is based on a single radial SimBench network. While this feeder provides a realistic and reproducible benchmark, distribution networks differ considerably in topology, customer composition, and electrical characteristics. Consequently, the quantitative findings should not be generalized to all Dutch low-voltage networks without further validation on additional network models.

Second, the demand model is derived from a single representative Dutch residential load profile, with stochastic variations introduced through an autoregressive process. Although this captures household demand variability, it does not explicitly represent the diversity of customer types that may be present in practical low-voltage networks, such as commercial buildings, schools, or industrial consumers.

Third, photovoltaic curtailment is represented as an economic penalty reflecting the opportunity cost of unused renewable generation. In practice, the financial consequences of curtailment depend on market mechanisms, contractual arrangements, and regulatory frameworks. The adopted formulation therefore represents an approximation rather than a direct operational cost.

Fourth, the optimization assumes perfect foresight of electricity demand, photovoltaic generation, and electricity prices over the entire optimization horizon. Real-world battery operation relies on forecasts that are inherently uncertain, which may reduce the achievable operational performance.

Fifth, the network is modeled using a balanced LinDistFlow approximation. Although this enables computationally efficient optimization over a full-year horizon, it neglects phase imbalance and certain nonlinear AC power flow characteristics that may become relevant in highly stressed low-voltage networks. A minor limitation concerns the state-of-charge indexing at the boundary of the optimization horizon. The SOC dynamics are applied from the second timestep onward, while the cyclic condition only equates the final and initial SOC levels. As a result, charging or discharging during the first timestep is not explicitly linked to an SOC update. This affects only a single hour within the full 8,760-hour horizon and is therefore expected to have a negligible effect on the reported results, but a future implementation should include an explicit wraparound SOC update.

Finally, the optimization considers battery storage as the sole congestion management measure. Other flexibility options, such as demand response, network reconfiguration, transformer upgrades, or conventional grid reinforcement, are outside the scope of this research but could provide complementary solutions within integrated network planning.

7

Conclusion

The increasing electrification of society and the rapid integration of distributed photovoltaic generation are placing increasing pressure on low-voltage electricity networks. Battery Energy Storage Systems have emerged as a promising flexibility resource to alleviate congestion, yet determining where batteries should be installed, how large they should be, and how they should be operated remains a complex optimization problem. This research addressed this challenge by developing a mixed-integer linear optimization framework that jointly determines the optimal placement, sizing, and operation of battery storage while explicitly considering voltage constraints, line loading, photovoltaic generation, and electricity market conditions.

The results demonstrate that, for the evaluated network, battery storage can effectively support congestion management, although its effectiveness depends strongly on the underlying network characteristics. The optimization consistently identified the same electrically weak feeder-end locations as the most suitable battery sites, suggesting that network topology is the primary driver of battery placement within the evaluated network. In contrast, optimal battery capacities adapted to increasing electrification levels and photovoltaic penetration, highlighting the importance of endogenous storage sizing within planning models. This distinction between robust battery placement and adaptive battery sizing emerged as one of the central findings of this study.

Furthermore, battery storage was found to provide predominantly local congestion relief. Strategically placed batteries improved voltage margins, reduced voltage stress at electrically weak buses, reduced loading on nearby distribution lines, and increased the utilization of locally generated photovoltaic energy. However, storage did not eliminate the structural network constraints observed in the evaluated network. Significant photovoltaic curtailment remained under high penetration scenarios, while the most heavily loaded line continued to determine the loading limits of the network. These findings indicate that, within the scope of this study, battery storage should be regarded as a complementary flexibility measure rather than a complete substitute for conventional grid reinforcement.

Finally, the economic sensitivity analysis demonstrated that the technical value of battery storage and its economic attractiveness are driven by different factors. While the technically optimal battery placement and sizing remained unchanged throughout the sensitivity analysis, the economic performance varied substantially under different electricity market conditions. When excluding the modeling penalty associated with avoided photovoltaic curtailment, battery storage was economically attractive only during periods of high electricity price volatility. This emphasizes that future investment decisions should consider both the technical value of storage for congestion management and the economic opportunities created by evolving electricity markets.

Overall, this research demonstrates the potential of optimization-based battery planning to support distribution system operators in identifying storage locations that provide high technical value while balancing operational and investment costs. Although the results are based on a single Dutch low-voltage distribution network, they illustrate how optimization models can support more targeted and economically informed storage planning. As low-voltage networks continue to accommodate increasing electrification and renewable generation, such planning tools may contribute to more effective congestion management by jointly considering technical network constraints and economic operating conditions.

References

[1] Timur Yunusov, Damien Frame, William Holderbaum, and Ben Potter. **The impact of location and type on the performance of low-voltage network connected battery energy storage systems**. **165**:202–213. 1, 9, 10, 86

[2] Noman Shabbir, Lauri Kütt, Victor Astapov, Kamran Daniel, Muhammad Jawad, Oleksandr Husev, Argo Rosin, and João Martins. **Enhancing PV hosting capacity and mitigating congestion in distribution networks with deep learning based PV forecasting and battery management**. **372**:123770. 1, 2, 5, 6, 7, 8, 9, 86, 87, 88, 89

[3] Dong Zhang, G.M. Shafiullah, Choton K. Das, and Kok Wai Wong. **Optimal allocation of battery energy storage systems to improve system reliability and voltage and frequency stability in weak grids**. **377**:124541. 1, 9, 86, 87, 88, 89

[4] Leandro Lind, Rafael Cossent, and Pablo Frías. **TSO-DSO Coordination for the Procurement of Balancing and Congestion Management Services: Assessment of a meshed-to-meshed topology**. 1

[5] Samar Fatima, Verner Püvi, and Matti Lehtonen. **Comparison of Different References When Assessing PV HC in Distribution Networks**. **3**(1):123–137. 1, 2, 5, 6, 12, 86

[6] Ricardo Torquato, Diogo Salles, Caio Oriente Pereira, Paulo Cesar Magalhaes Meira, and Walmir Freitas. **A Comprehensive Assessment of PV Hosting Capacity on Low-Voltage Distribution Systems**. **33**(2):1002–1012. 2, 5, 6, 12, 86

[7] Manar A. Khalil, Tamer M. Elkhodragy, and Waleed A. A. Salem. **A novel hybrid algorithm based on optimal size and location of photovoltaic

with battery energy storage systems for voltage stability enhancement. **107**(1):1009–1034. 2, 7, 8, 39, 86

[8] Andrea Mazza, Hamidreza Mirtaheri, Gianfranco Chicco, Angela Russo, and Maurizio Fantino. **Location and Sizing of Battery Energy Storage Units in Low Voltage Distribution Networks**. **13**(1):52. 2, 8, 9, 14

[9] Mohammad Rasol Jannesar, Alireza Sedighi, Mehdi Savaghebi, and Josep M. Guerrero. **Optimal placement, sizing, and daily charge/discharge of battery energy storage in low voltage distribution network with high photovoltaic penetration**. **226**:957–966. 2, 10, 88

[10] Xuan Wu, Rajarshi Roychowdhury, Hui Zhang, Barry Feldman, and Raiford Smith. **Optimal BESS Sizing for PV Interconnection & Energy Arbitrage with Industrial Customers**. In *2024 IEEE Power & Energy Society General Meeting (PESGM)*, pages 1–5. IEEE. 2, 12, 13

[11] Ye Yang, Hui Li, Andreas Aichhorn, Jianping Zheng, and Michael Greenleaf. **Sizing Strategy of Distributed Battery Storage System With High Penetration of Photovoltaic for Voltage Regulation and Peak Load Shaving**. **5**(2):982–991. 2, 5, 7, 8, 9, 10, 13

[12] Partha Kayal, Bablu Kumar, and Soumyakanta Samantary. **Allocation of battery energy storage in power distribution network: Placement, sizing, and scheduling**. **44**(3):7544–7563. 2, 9

[13] Jamshid Aghaei, Seyed Aboozar Bozorgavari, Sasan Pirouzi, Hossein Farahmand, and Magnus Korpås. **Flexibility Planning of Distributed Battery Energy Storage Systems in Smart Distribution Networks**. **44**(3):1105–1121. 2, 12

[14] Werner van Westering and Hans Hellendoorn. **Low voltage power grid congestion reduction using a community battery_ Design principles, control and experimental validation**. **144**(105349). 5

[15] Juan Francisco Piedra-Segura, Gustavo Adolfo Gomez-Ramirez, Oscar Nunez-Mata, and Fausto Calderon-Obaldia. **Trends and Outlook of BESS in Electrical Grids of Latin America**. IEEE Xplore. 6

[16] H.S. Salama and I. Vokony. **Voltage stability indices-A comparison and a review**. **98**. 8

[17] N.S. Wade, P.C. Taylor, P.D. Lang, and P.R. Jones. **Evaluating the benefits of an electrical energy storage system in a future smart grid**. **38**(11):7180–7188. 8, 10

[18] Raju Wagle, Pawan Sharma, Charu Sharma, and Mohammad Amin. **Optimal power flow based coordinated reactive and active power control to mitigate voltage violations in smart inverter enriched distribution network**. **21**(2):359–375. 9, 10

[19] Sezen Ece Kayacik, Albert H. Schrotenboer, Evrim Ursavas, and Iris F.A. Vis. **Towards low-carbon power networks: Optimal location and sizing of renewable energy sources and hydrogen storage**. **38**:101394. 9

[20] Adedoyin Inaolaji, Xuan Wu, Rajarshi Roychowdhury, and Raiford Smith. **Optimal allocation of battery energy storage systems for peak shaving and reliability enhancement in distribution systems**. **95**:11. 9, 11, 12, 13

[21] Alejandro Valencia, Ricardo A. Hincapie, and Ramón A. Gallego. **Optimal location, selection, and operation of battery energy storage systems and renewable distributed generation in medium–low voltage distribution networks**. **34**:102158. 10, 11, 12, 13

[22] Remy Rigo-Mariani and Vannak Vai. **An Iterative Linear DistFLow for Dynamic Optimization in Distributed Generation Planning Studies**. **138**. 10

[23] César Cienfuegos. **Comparative analysis of battery energy storage systems' operation strategies for peak shaving in industries with or without installed photovoltaic capacity**. **49**(100574). 11

[24] Ruoxuan Leng, Zhengmao Li, and Yan Xu. **A Comprehensive Literature Review for Optimal Planning of Distributed Energy Resources in Distribution Grids**. In *2022 IEEE PES Innovative Smart Grid Technologies - Asia (ISGT Asia)*, pages 369–373. IEEE. 11

[25] Bahman Khaki. **Joint sizing and placement of battery energy storage systems and wind turbines considering reactive power support of the system**. **35**:102264. 11

[26] Yujie Tang. **Optimal Placement of Energy Storage in Distribution Networks**. **8**(6):3094 – 3103. 11

[27] Mesut Baran and Felix Wu. **Network Reconfiguration in distrubution system for loss reduction and load balancing**. **4**(2):7. 12, 21

[28] Umesh Kumar Das. **Analysis of Distribution Transformer Overload Management Using Battery Energy Storage System**. Number 73. 12

[29] Philipp Fortenbacher, Martin Zellner, and Göran Andersson. **Optimal Sizing and Placement of Distributed Storage in Low Voltage Networks**. In *2016 Power Systems Computation Conference (PSCC)*, pages 1–7. 12

[30] José Iria, Miguel Heleno, and Gonçalo Candoso. **Optimal sizing and placement of energy storage systems and on-load tap changer transformers in distribution networks**. 12

[31] Ruotong Sun, Ermin Wei, and Lihui Yi. **Optimal Battery Placement in Power Grid**. 12

8

Appendix

Bus-Level Annual Demand Allocation

Bus	Annual Demand [MWh/year]	Color	Bus	Annual Demand [MWh/year]	Color
40	49.473	dark-red	6	2.444	yellow
34	47.776	dark-red	7	2.444	yellow
39	46.007	dark-red	22	2.444	yellow
35	42.173	dark-red	24	2.444	yellow
38	32.878	dark-red	3	2.327	yellow
36	30.914	dark-red	8	2.327	yellow
41	19.568	dark-orange	9	2.327	yellow
18	12.042	dark-orange	21	2.327	yellow
42	11.892	dark-orange	11	1.984	yellow
16	7.332	dark-orange	15	1.984	yellow
2	4.888	light-orange	32	1.984	yellow
19	4.888	light-orange	29	1.833	yellow
30	4.888	light-orange	33	1.833	yellow
4	4.653	light-orange	13	1.488	yellow
25	4.653	light-orange	1	0.000	none
20	3.815	light-orange	14	0.000	none
5	3.666	light-orange	17	0.000	none
27	3.666	light-orange	37	0.000	none
10	3.666	light-orange			
28	3.321	light-orange			
0	3.102	light-orange			
26	3.102	light-orange			
31	3.102	light-orange			
12	2.976	light-orange			
23	2.976	light-orange			

Table 8.1: Annual energy demand per bus (E_i^{year}) in MWh per year, including visualization color category from Figure 4.1.

Full year of electricity pricing for the year 2025

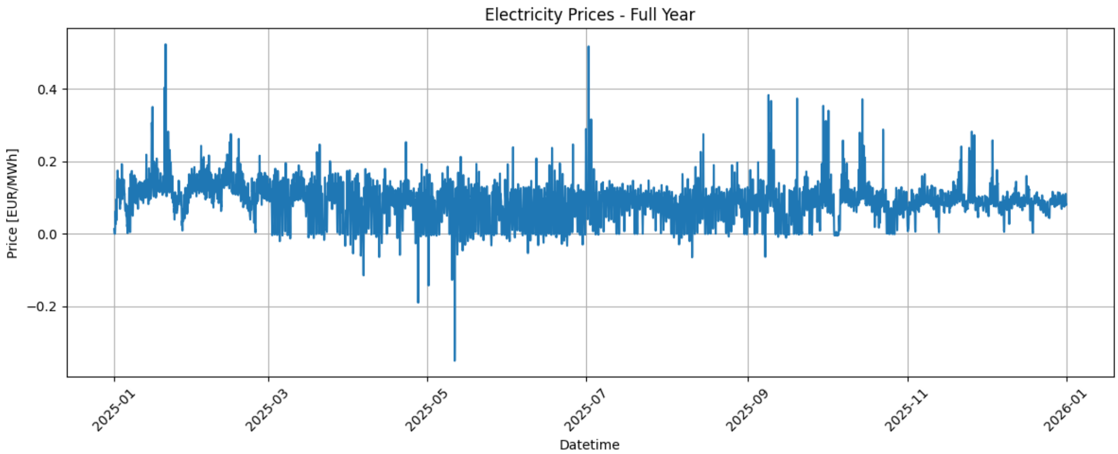

Figure 8.1: Hourly Dutch day-ahead electricity prices during the year 2025.

Analysis of bus ranking voltage problems without batteries

Table 8.2: Most critical buses ranked by minimum voltage in the baseline scenario (RQ1.2, no BESS, electrification factor 1.25, PV factor 1.12).

Rank	Bus	Min Voltage	P1 Voltage	Mean Voltage	Voltage Range
1	39	0.9703	0.9830	1.0140	0.0572
2	38	0.9712	0.9837	1.0141	0.0557
3	42	0.9715	0.9836	1.0141	0.0550
4	41	0.9717	0.9838	1.0142	0.0546
5	40	0.9722	0.9843	1.0143	0.0540
6	37	0.9743	0.9859	1.0147	0.0510
7	36	0.9774	0.9883	1.0153	0.0476
8	35	0.9839	0.9931	1.0165	0.0411
9	34	0.9897	0.9977	1.0177	0.0353
10	25	0.9988	1.0034	1.0191	0.0284

Table 8.3: Most critical buses ranked by minimum voltage in the baseline scenario (Propotional PV deployment, PV factor 2.00, no BESS).

Rank	Bus	Min Voltage	P1 Voltage	Mean Voltage	Voltage Range
1	39	0.9815	0.9916	1.0164	0.0457
2	38	0.9822	0.9921	1.0165	0.0444
3	42	0.9824	0.9920	1.0165	0.0435
4	41	0.9826	0.9922	1.0166	0.0432
5	40	0.9830	0.9926	1.0167	0.0428
6	37	0.9846	0.9939	1.0170	0.0406
7	36	0.9871	0.9958	1.0174	0.0379
8	35	0.9923	0.9996	1.0184	0.0327
9	34	0.9969	1.0032	1.0193	0.0281
10	25	1.0041	1.0077	1.0204	0.0234

Table 8.4: Most critical buses ranked by minimum voltage in the baseline scenario (Line-based PV deployment, PV factor 2.00, no BESS).

Rank	Bus	Min Voltage	P1 Voltage	Mean Voltage	Voltage Range
1	39	0.9815	0.9916	1.0162	0.0435
2	38	0.9822	0.9921	1.0163	0.0428
3	42	0.9824	0.9920	1.0163	0.0426
4	41	0.9826	0.9922	1.0164	0.0424
5	40	0.9830	0.9926	1.0165	0.0420
6	37	0.9846	0.9939	1.0168	0.0404
7	36	0.9871	0.9958	1.0173	0.0379
8	35	0.9923	0.9996	1.0184	0.0327
9	34	0.9969	1.0032	1.0193	0.0281
10	6	1.0044	1.0080	1.0204	0.0227

Table 8.5: Most critical buses ranked by minimum voltage in the baseline scenario (Bus-based PV deployment, PV factor 2.00, no BESS).

Rank	Bus	Min Voltage	P1 Voltage	Mean Voltage	Voltage Range
1	39	0.9815	0.9916	1.0166	0.0456
2	42	0.9824	0.9920	1.0168	0.0451
3	38	0.9822	0.9922	1.0167	0.0444
4	41	0.9826	0.9922	1.0168	0.0444
5	40	0.9830	0.9926	1.0169	0.0433
6	37	0.9846	0.9939	1.0172	0.0407
7	36	0.9871	0.9958	1.0176	0.0379
8	35	0.9923	0.9996	1.0185	0.0327
9	34	0.9969	1.0032	1.0193	0.0281
10	25	1.0041	1.0077	1.0207	0.0270

Bus ranking based on line loadings in scenarios without BESS

Table 8.6: Most critical lines ranked by P99 loading in the RQ1.2 scenario (electrification factor 1.25, no BESS).

Rank	From	To	Mean (%)	P95 (%)	P99 (%)	Max (%)
1	14	34	20.13	55.67	75.22	99.49
2	34	35	16.96	46.24	62.75	78.83
3	35	36	14.02	38.20	51.67	68.70
4	129	14	12.79	36.02	48.62	61.23
5	36	37	11.86	31.68	43.07	55.69
6	14	20	6.41	16.88	22.92	27.09
7	37	40	6.16	16.22	22.08	29.74
8	20	7	6.13	16.13	21.86	25.65
9	37	38	6.14	15.63	21.44	27.61
10	7	31	5.95	15.64	21.25	25.06

Table 8.7: Most critical lines ranked by P99 loading in the Propotional PV deployment scenario (PV factor 2.00, no BESS).

Rank	From	To	Mean (%)	P95 (%)	P99 (%)	Max (%)
1	14	34	15.79	44.35	60.16	79.57
2	34	35	13.41	36.83	50.18	63.05
3	35	36	11.10	30.22	41.32	54.95
4	129	14	9.92	28.59	38.88	48.97
5	36	37	9.41	25.21	34.44	44.54
6	14	20	5.14	13.38	18.33	21.67
7	37	40	4.90	12.94	17.66	23.78
8	20	7	4.92	12.75	17.48	20.52
9	37	38	4.95	12.82	17.16	22.08
10	7	31	4.78	12.38	16.99	20.04

Table 8.8: Most critical lines ranked by P99 loading in the Bus-based PV deployment scenario (PV factor 2.00, no BESS).

Rank	From	To	Mean (%)	P95 (%)	P99 (%)	Max (%)
1	14	34	15.74	44.39	60.16	79.58
2	34	35	13.20	36.80	50.18	63.05
3	35	36	11.08	30.17	41.31	54.95
4	129	14	9.91	28.59	38.88	48.97
5	36	37	9.44	25.08	34.44	44.54
6	14	20	5.18	13.58	18.38	21.66
7	37	40	4.99	13.13	17.66	23.78
8	20	7	4.98	13.01	17.56	20.51
9	37	38	5.00	12.86	17.18	22.08
10	7	31	4.85	12.71	17.07	20.03

Table 8.9: Most critical lines ranked by P99 loading in the Line-based PV deployment scenario (PV factor 2.00, no BESS).

Rank	From	To	Mean (%)	P95 (%)	P99 (%)	Max (%)
1	14	34	15.89	44.29	60.16	79.57
2	34	35	13.74	36.89	50.19	63.06
3	35	36	11.35	30.49	41.33	54.96
4	129	14	9.91	28.59	38.88	48.97
5	36	37	9.73	25.41	34.46	44.56
6	14	20	5.63	13.45	18.33	21.67
7	37	40	4.94	12.96	17.67	23.79
8	20	7	5.40	12.79	17.48	20.52
9	37	38	4.87	12.42	17.16	22.09
10	7	31	5.17	12.51	17.00	20.05

PV sensitivity battery placement

Table 8.10: Optimal BESS placement and sizing under different PV allocation strategies.

Strategy	PV Factor	BESS Budget	Bus	Energy [kWh]	Power [kW]
Proportional PV Allocation					
Proportional	1.00	1	24	101.83	25.46
Proportional	1.00	2	3	29.85	7.46
Proportional	1.00	2	39	71.98	18.00
Proportional	1.25	1	29	137.62	34.40
Proportional	1.25	2	22	61.22	15.30
Proportional	1.25	2	24	76.40	19.10
Proportional	1.50	1	25	177.18	44.29
Proportional	1.50	2	3	81.93	20.48
Proportional	1.50	2	39	95.25	23.81
Proportional	1.75	1	25	203.86	50.97
Proportional	1.75	2	3	104.48	26.12
Proportional	1.75	2	39	99.38	24.85
Proportional	2.00	1	25	230.99	57.75
Proportional	2.00	2	3	110.01	27.50
Proportional	2.00	2	39	120.98	30.24
Voltage-Severity-Based Allocation					
Bus	1.00	1	26	101.83	25.46
Bus	1.00	2	3	45.23	11.31
Bus	1.00	2	39	56.60	14.15
Bus	1.25	1	27	137.62	34.40
Bus	1.25	2	0	61.67	15.42
Bus	1.25	2	5	75.95	18.99
Bus	1.50	1	25	177.18	44.29

Continued on next page

Table 8.10 – continued from previous page

Strategy	PV Factor	BESS Budget	Bus	Energy [kWh]	Power [kW]
Bus	1.50	2	12	177.18	44.29
Bus	1.75	1	25	203.86	50.97
Bus	1.75	2	3	105.68	26.42
Bus	1.75	2	39	98.18	24.55
Bus	2.00	1	26	230.99	57.75
Bus	2.00	2	3	121.96	30.49
Bus	2.00	2	39	109.03	27.26
NLSI-Based Allocation					
Line	1.00	1	25	101.83	25.46
Line	1.00	2	3	50.45	12.61
Line	1.00	2	39	51.38	12.85
Line	1.25	1	24	137.62	34.40
Line	1.25	2	3	62.55	15.64
Line	1.25	2	39	75.07	18.77
Line	1.50	1	24	177.18	44.29
Line	1.50	2	3	82.78	20.70
Line	1.50	2	39	94.39	23.60
Line	1.75	1	25	203.86	50.97
Line	1.75	2	1	88.92	22.23
Line	1.75	2	4	114.94	28.74
Line	2.00	1	25	230.99	57.75
Line	2.00	2	3	108.40	27.10
Line	2.00	2	39	122.59	30.65

Results PV sensitivity analysis - Curtailment

Table 8.11: PV utilization and curtailment results for all RQ2 scenarios.

PV Factor	Strategy	B0 Used (%)	B0 Curt. (%)	B1 Used (%)	B1 Curt. (%)	B2 Used (%)	B2 Curt. (%)
PV100	Propotional	19.30	80.70	25.02	74.98	25.02	74.98
	Bus	19.35	80.65	25.02	74.98	25.02	74.98
	Line	19.33	80.67	25.02	74.98	25.01	74.99
PV125	Propotional	16.76	83.24	23.17	76.83	23.17	76.83
	Bus	16.82	83.18	23.16	76.84	23.16	76.84
	Line	16.79	83.21	23.17	76.83	23.14	76.86
PV150	Propotional	14.89	85.11	21.94	78.06	21.94	78.06
	Bus	14.95	85.05	21.94	78.06	21.93	78.07
	Line	14.93	85.07	21.91	78.09	21.92	78.08
PV175	Propotional	13.44	86.56	20.56	79.44	20.55	79.45
	Bus	13.48	86.52	20.56	79.44	20.55	79.45
	Line	13.46	86.54	20.55	79.45	20.54	79.46
PV200	Propotional	12.25	87.75	19.46	80.54	19.46	80.54
	Bus	12.30	87.70	19.46	80.54	19.46	80.54
	Line	12.28	87.72	19.46	80.54	19.46	80.54